Laminar flow over unsteady humps: the formation of waves

By P. W. DUCK

Department of Mathematics, University of Manchester, Manchester M13 9PL

Both the incompressible and supersonic laminar flow over a small, unsteady hump are considered. The Reynolds number is assumed large, and the analysis is based upon triple-deck theory. In the incompressible case disturbances tend to grow downstream, as a result of triggering the Tollmien–Schlichting mode of instability. For the supersonic case the flow disturbances tend to decay downstream across the entire frequency spectrum. However, for sufficiently large humps a seemingly catastrophic failure of the governing equations may occur, our results suggesting that this is caused by an inviscid, short-scale, Rayleigh type of instability.

1. Introduction

In this paper we consider the problem of the interaction between an otherwise steady laminar boundary layer on a flat plate, and a small unsteady surface distortion of the plate. This problem was posed by Duck (1978), hereinafter referred to as I, who solved the problem asymptotically in the limit of increasingly fast oscillations of the perturbation. This work in turn was based on the (completely) steady work of Smith (1973). The three-dimensional analogue to I was considered by Duck (1981).

We shall keep the formulation of the problem to a minimum – a full description is given in I. Suppose U_∞ is the free-stream velocity, L some characteristic lengthscale (typically the distance between the hump and the leading edge of the plate), ν the kinematic viscosity, and $1/\Omega$ is a characteristic timescale associated with the unsteadiness. We may now define two non-dimensional parameters: first, a Reynolds number $R = U_\infty L/\nu$, which is assumed large; and, secondly, $\beta_0 = [U_\infty/\Omega L]^{\frac{1}{2}}$, an unsteadiness parameter (associated with the Strouhal number).

Taking our origin of coordinates suitably near the wall distortion, we define our dimensional coordinates Lx, Ly parallel and perpendicular to the streamwise direction respectively.

Using the non-dimensionalization of I for the dependent variables allows us to write the Navier–Stokes equations in the form

$$\frac{1}{\beta_0^2}\frac{\partial \boldsymbol{u}}{\partial t}+(\boldsymbol{u}\cdot\boldsymbol{\nabla})\,\boldsymbol{u} = -\boldsymbol{\nabla}p+\frac{1}{R}\,\nabla^2\boldsymbol{u}, \tag{1.1}$$

$$\boldsymbol{\nabla}\cdot\boldsymbol{u} = 0, \tag{1.2}$$

where $\boldsymbol{u} = (u, v)$ is the velocity vector, and p the pressure.

As in much multi-layered (or 'triple-deck') analysis, we find it helpful to define a small parameter, based on the Reynolds number, namely

$$\epsilon = R^{-\frac{1}{8}}. \tag{1.3}$$

Following I (and other triple-deck work) we suppose that the distortion profile is given by

$$y = \epsilon^5 hF(X,t),$$

with
$$X = x/\epsilon^3,$$
(1.4)

and where $hF(X,t)$ and X are generally $O(1)$ quantities.

In I, three distinct regimes of β_0 were considered (each based on a power of the Reynolds number). Of these perhaps the most interesting was the first considered:

$$\beta_0 = \epsilon\beta, \quad \beta = O(1),$$
(1.5)

which (with $Y = y/\epsilon^5 - hF(X,t)$) yields the following nonlinear boundary-layer problem:

$$\frac{1}{\beta^2}\,\Psi_{Yt} + \Psi_Y\,\Psi_{XY} - \Psi_X\,\Psi_{YY} = -P_X + \Psi_{YYY},$$
(1.6)

where $\epsilon^6\psi(X,Y,t)$ is the non-dimensional stream function, and $\epsilon^2 P(X,t)$ is the non-dimensional pressure. The boundary conditions which must be applied to (1.6) are

$$\Psi(Y=0) = \Psi_Y(Y=0) = 0,$$
(1.7a)

$$\Psi_Y \to Y + A(X,t) + hF(X,t) \quad \text{as } Y \to \infty.$$
(1.7b)

(Here we have assumed that a simple renormalization of the variables has been carried out in order to set the value of the wall shear of the oncoming, undisturbed boundary layer to unity). $A(X,t)$ is a displacement function which is to be determined. The final condition that closes the problem arises from the 'upper deck', and in the case of incompressible flows is

$$\frac{\partial A}{\partial X} = -\frac{1}{\pi}\int_{-\infty}^{\infty}\frac{P(\xi,t)}{X-\xi}\,\mathrm{d}\xi.$$
(1.8)

We also propose to study supersonic flows, in which case the following relationship applies

$$P(X,t) = -A_X(X,t).$$
(1.9)

In I the limit of $\beta \to 0$ was taken ($\beta \to \infty$ leads to a quasi-steady solution, based on the steady solution of Smith 1973). In this paper we concentrate on the 'order-one' problem.

We believe that a study of the system (1.6) is important for the following reasons. Physically we may interpret the problem as modelling the well-known vibrating-ribbon experiment used in investigating boundary-layer stability (and transition), one of the most important (and vexing) questions in fluid mechanics. It has been shown by Smith (1979a,b) that a fully rational description of linear and weakly nonlinear stability theory (see Lin 1955 and Stuart 1960, Watson 1960 respectively) may be expressed compactly within the context of triple-deck theory, similar to that described above. In the case of weakly nonlinear theory (for example Smith 1979a) the analysis applies to small disturbances which are very slightly supercritical (according to linear theory). This weakly nonlinear theory predicts that nonlinear effects have a stabilizing influence on the flow in the immediate vicinity of the neutral curve. One of the aims of this paper is to demonstrate this effect numerically, whilst at the same time investigating 'order-one' disturbances (on the scale of the lower deck), not necessarily very close to a neutral point.

The inherent connection between a harmonic oscillator on a steady viscous flow and the hydrodynamic-stability problem (in channel flows) has recently been verified by Bogdanova & Ryzhov (1983), who also based their analysis on multi-layered arguments. Using linearized analysis, these authors showed how, above a critical frequency of oscillation, the (lower-branch Tollmien–Schlichting) waves triggered by the oscillator cease to decay downstream.

Assuming this connection between a forced oscillation on the boundary layer and boundary-layer stability, in this paper we study the external-flow problem analogous to that of Bogdanova & Ryzhov (1983). However, in our case we study the fully nonlinear system (1.6). As $h \to 0$ we may expect to retrieve the results of a linearized analysis, whilst it is the $h = O(1)$ results that are likely to be the most interesting.

Finally, we note that we shall be focusing our attention on regions in parameter space fairly close to the lower (Tollmien–Schlichting) branch. It is this branch (rather than the upper branch) that is likely to be of more practical importance since it is encountered first in practical situations.

The layout of the paper is as follows: in the next section we consider the linearized solution ($h \to 0$) of (1.6), which will guide our investigation of the full, nonlinear system (using the method described in §3). Our results are presented in §4, and our conclusions are given in §5.

2. Linearized solutions

We first seek solutions of (1.6) as $h \to 0$, assuming $F(X, t)$ takes on a simple periodic form in time. This analysis is likely to give us a good indication of many of the features of the nonlinear solutions to be obtained later.

We first differentiate (1.6) with respect to Y, to eliminate the pressure term, obtaining

$$\frac{1}{\beta^2} \Psi_{YYt} + \Psi_Y \Psi_{XYY} - \Psi_X \Psi_{YYY} = \Psi_{YYYY}. \tag{2.1}$$

Next, we define a (perturbation) shear stress $\hat{\tau} = (\Psi_{YY} - 1)/h$. If we then neglect the nonlinear terms ($O(h^2)$) in (2.1), the resulting system is

$$\frac{1}{\beta^2} \hat{\tau}_t + Y\hat{\tau}_X - \hat{\tau}_{YY} = 0. \tag{2.2}$$

If we also neglect transients, leaving a purely time-periodic solution, then we may write

$$\hat{\tau} = \bar{\tau} \, \mathrm{e}^{\mathrm{i}t} + \text{c.c.}, \quad F = f \mathrm{e}^{\mathrm{i}t} + \text{c.c.}, \tag{2.3}$$

where $\bar{\tau}$ is described by

$$\frac{\mathrm{i}\bar{\tau}}{\beta^2} + Y\bar{\tau}_X - \bar{\tau}_{YY} = 0. \tag{2.4}$$

Taking the Fourier transform of (2.4), with respect to X, gives

$$\left(\frac{\mathrm{i}}{\beta^2} + \mathrm{i}k Y\right) \bar{\tau}^* - \bar{\tau}^*_{YY} = 0, \tag{2.5}$$

where

$$\bar{\tau}^*(k, Y) = \int_{-\infty}^{\infty} \bar{\tau}(X, Y) \, \mathrm{e}^{-\mathrm{i}kX} \, \mathrm{d}X. \tag{2.6}$$

Imposing the conditions (1.7) yields the following solution for $\bar{\tau}^*$,

$$\bar{\tau}^* = \frac{ikAf^* \, \mathrm{Ai}\left\{(ik)^{\frac{1}{3}}\left(Y + \dfrac{1}{k^2\beta}\right)\right\}}{(ik)^{\frac{2}{3}} \varLambda \displaystyle\int_{(ik)^{\frac{1}{3}}/\beta^2 k}^{\infty} \mathrm{Ai}\,(\zeta)\,\mathrm{d}\zeta - (ik)^{\frac{1}{3}}\,\mathrm{Ai}'\left[\dfrac{(ik)^{\frac{1}{3}}}{\beta^2 k}\right]} \tag{2.7}$$

(where $P^* = \varLambda(k)\,A^*$ is the transform of the pressure/displacement relationship).

If we use complex-variable methods then the inversion of this expression, in general, comprises two distinct contributions. The first comes from integrals along either side of any branch cuts, which is the continuous-spectrum component of the inversion. For the purposes of (2.7), we must have

$$-\tfrac{3}{2}\pi < \arg\,(k) < \tfrac{1}{2}\pi \tag{2.8}$$

in order that the Airy function is bounded as $Y \to \infty$, yielding one branch cut. For the incompressible case, we also have branch cuts along both imaginary axes, since

$$\left.\begin{aligned}\varLambda(k) &= k, \quad \mathrm{Re}\,(k) > 0, \\ &= -k, \quad \mathrm{Re}\,(k) < 0.\end{aligned}\right\} \tag{2.9a}$$

For supersonic flows $\qquad\qquad \varLambda(k) = -ik, \quad \text{for all } k. \tag{2.9b}$

The second and discrete contribution in the inversion of (2.7) arises from the residues from any poles in the complex-k-plane. We shall see that these are crucial in the present problem. These poles occur whenever we have

$$(ik)^{\frac{1}{3}}\varLambda \int_{(ik)^{\frac{1}{3}}/\beta^2 k}^{\infty} \mathrm{Ai}\,(\zeta)\,\mathrm{d}\zeta = \mathrm{Ai}'\left[\frac{(ik)^{\frac{1}{3}}}{\beta^2 k}\right]. \tag{2.10}$$

Equation (2.10) was solved for both the supersonic and incompressible cases for a range of $\beta > 0$, and the roots in the complex plane are shown in figures 1 and 2 respectively. Note that Zhuk & Ryzhov (1978), Terent'ev (1978) and Ryzhov & Zhuk (1980) have considered various aspects of the supersonic problem, but do not appear to have treated this aspect in any detail.

There are a number of interesting features on these figures. First, in the supersonic case, it appears that, if $k = -k_r + ik_i$ (k_r, $k_i > 0$, real), is a root in the second quadrant, then so too is $k = -k_i + ik_r$. Also, for a given value of β, then there exist many roots of this type in the second quadrant (just the first three are shown in figure 1). Further the line $\mathrm{Re}\,(k) = -\mathrm{Im}\,(k)$ in this quadrant is itself a (continuous) line of roots; indeed, it appears that, generally, for a given value of β there exist many values of k satisfying (2.10) on this line (these features are confirmed below).

We may study both these sets of roots, asymptotically, following the work of Ryzhov & Zhuk (1980).

Defining, for convenience,

$$\zeta = \frac{(ik)^{\frac{1}{3}}}{\beta^2 k}, \tag{2.11}$$

then (2.10) may be written

$$-(ik)^{\frac{4}{3}} \int_{\zeta}^{\infty} \mathrm{Ai}\,(\zeta)\,\mathrm{d}\zeta = \mathrm{Ai}'\,(\zeta). \tag{2.12}$$

For this (supersonic) case, we may show that as $|\zeta| \to \infty$, (2.12) possesses an infinite number of roots on and in the vicinity of $\arg \zeta = \pi$, corresponding to $\arg k = -\tfrac{5}{4}\pi$.
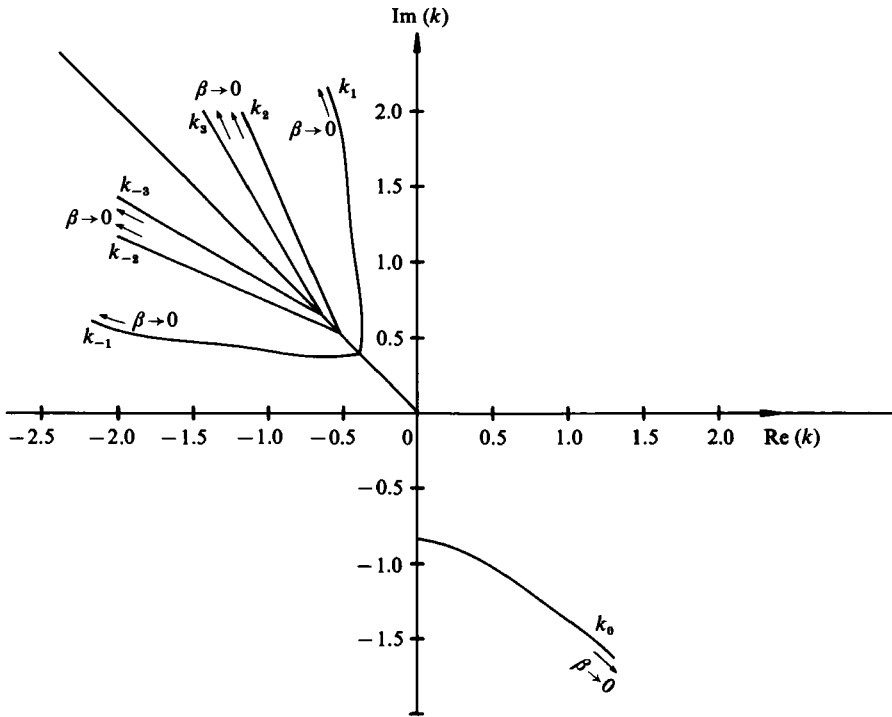
FIGURE 1. Roots of (2.12), β prescribed, supersonic case.

More precisely, we write

$$\zeta = |\zeta| e^{i(\pi - \theta')}, \tag{2.13}$$

where $\theta' \ll 1$, and hence we must have (for β real)

$$k = |k| e^{-\frac{5}{4}i\pi - \frac{3}{2}i\theta'}. \tag{2.14}$$

As $|\zeta| \to \infty$, we may use the asymptotic behaviour of the Airy function, close to the negative real axis of ζ, to give the following asymptotic form for (2.12)

$$|\zeta|^{\frac{1}{4}} \cos\left[\tfrac{2}{3}|\zeta|^{\frac{3}{2}} + \tfrac{1}{4}\pi\right] - i\theta' |\zeta|^{\frac{1}{4}} \sin\left[\tfrac{2}{3}|\zeta|^{\frac{3}{2}} + \tfrac{1}{4}\pi\right] = -\pi^{\frac{1}{2}} |k|^{\frac{3}{2}}[1 - 2i\theta']. \tag{2.15}$$

First, assuming $\theta' = 0$, i.e. considering roots lying on the line $\arg(k) = -\tfrac{5}{4}\pi$, then the imaginary part of this equation is identically satisfied, whilst the remaining (real) equation is

$$|\zeta|^{\frac{1}{4}} \cos\left[\tfrac{2}{3}|\zeta|^{\frac{3}{2}} + \tfrac{1}{4}\pi\right] = -\pi^{\frac{1}{2}} |k|^{\frac{3}{2}}. \tag{2.16}$$

As $|\zeta| \to \infty$, $|k| = o(|\zeta|^{\frac{3}{16}})$, the solution of this equation is

$$|\zeta| = [\tfrac{3}{2}n\pi - \tfrac{9}{8}\pi]^{\frac{2}{3}}, \quad n \text{ positive, integer, and large}, \tag{2.17}$$

or

$$|k|^{\frac{3}{2}} \beta^2 = [\tfrac{3}{2}n\pi - \tfrac{9}{8}\pi]^{-\frac{1}{3}}. \tag{2.18}$$

This then indicates that for a given value of β there exist an infinite number of $|k|$ satisfying (2.12) on the line $\arg(k) = -\tfrac{5}{4}\pi$.

Let us now consider the case when $\theta' \neq 0$. Taking real and imaginary parts of (2.15) yields (2.16) (again), together with

$$|\zeta|^{\frac{1}{4}} \sin\left(\tfrac{2}{3}|\zeta|^{\frac{3}{2}} + \tfrac{1}{4}\pi\right) = -2\pi^{\frac{1}{2}} |k|^{\frac{3}{2}}. \tag{2.19}$$
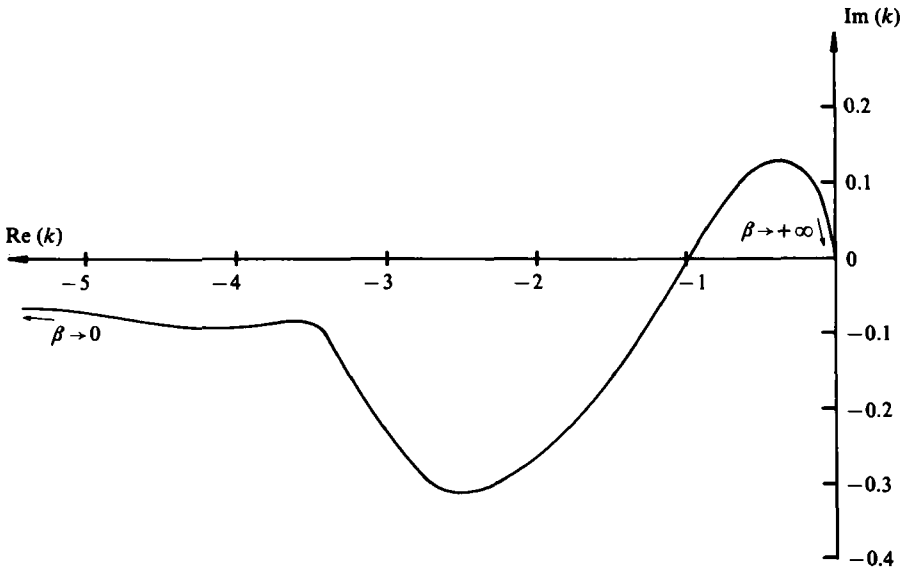
FIGURE 2. Roots of (4.21), β prescribed, incompressible case.

If we again take the limit $|\zeta| \to \infty$, and solve (2.16) in conjunction with (2.19), then

$$|k| = \pi^{-\frac{3}{8}}[3n\pi - \tfrac{15}{8}\pi]^{\frac{1}{8}},$$

$$\beta^2 = \pi^{\frac{1}{4}}[3n\pi - \tfrac{15}{8}\pi]^{-\frac{3}{4}}, \quad n \text{ positive, integer, and large.} \tag{2.20}$$

θ' remains arbitrary. This explains the occurrence of the roots $k_{\pm m}$ on figure 1.

In addition to these roots on and close to $\arg k = -\tfrac{5}{4}\pi$, there also exists a solitary root in the fourth quadrant, which approaches $k = -0.8272i$ as $\beta \to \infty$. It is the pole at this point that is responsible for the upstream influence in steady, supersonic, triple-deck flows (e.g. Stewartson & Williams 1969). Note that all these (discrete) contributions to the solution decay exponentially downstream.

Let us now consider what turns out to be the more interesting case, namely the incompressible example. In this case the equation determining the roots, namely (2.10), becomes

$$(ik)^{\frac{1}{4}}(k^2)^{\frac{3}{4}}\int_\zeta^\infty \mathrm{Ai}\,(\zeta)\,\mathrm{d}\zeta = \mathrm{Ai}'\,(\zeta), \tag{2.21}$$

with ζ defined by (2.11).

Equation (2.21) is the same equation obtained by a number of authors (e.g. Smith 1979a; Lin 1955) in the context of the hydrodynamic stability of boundary layers; however, these authors concerned themselves with the point of neutral stability, and hence required k to be real. The analogous system to (2.21) for channel flows was fully investigated by Bogdanova & Ryzhov (1983). Indeed, these latter results provided a useful check for the root-solving routine used by the author.

Figure 2 illustrates the roots of (2.21), and indicates that there exists just one (complex) value of k for a given value of β, in contrast to the non-uniqueness found in the supersonic case. The crucial feature of figure 2 is the cross-over of the negative real-k-axis at $\beta = \beta_c \approx 0.660$, $k = k_c \approx -1.000$. The reason for the importance of this is as follows. Ordinarily, if one is inverting a transformed variable, say $\bar{\tau}^*$, using complex-variable methods, then one takes a contour lying entirely within the lower

half of the k-plane to evaluate $\bar{\tau}$ for $X < 0$, whilst one takes a contour lying entirely within the upper half of the k-plane to determine $\bar{\tau}$ for $X > 0$. Consequently any poles in the lower half-plane contribute to the $X < 0$ solution, whilst any poles in the upper half-plane contribute to the $X > 0$ solution. This is the case in the present problem for $\beta > \beta_c$. However, as $\beta \to \beta_c +$, we see from figure 2 that a pole is approaching the negative real axis (from above), giving rise to a solution which, downstream, oscillates and decays progressively more slowly. If $\beta = \beta_c$, the solution in fact is purely oscillatory as $X \to \infty$. If we were to use our previously described criterion for inverting $\bar{\tau}^*$, then, as β is reduced below β_c, the solution as $X \to \infty$ would decay (without oscillation), whilst as $X \to -\infty$, the solution abruptly starts to oscillate. On physical grounds this description of the flow appears unlikely, owing to this discontinuity in solution.

As a result, we must redefine our choice of contours for $\beta < \beta_c$. Instead, for $X > 0$, we choose a contour as before, except with a detour into the lower half of the complex-k-plane to include this pole. This then excludes any contribution from this pole for $X < 0$. The result of this is that the solution varies continuously with β, as β reduces below β_c, and most importantly the solution grows exponentially (and oscillates) as $X \to \infty$.

The connection with the linear hydrodynamic stability of the boundary layer is now clear. $\beta = \beta_c$ corresponds to the point of neutral stability. If $\beta < \beta_c$ the unstable modes are excited by the hump oscillation, and lead to growing Tollmien–Schlichting waves downstream. We may state the condition for instability as follows (if $k = k_r + ik_i$): we require that $\partial k_r / \partial \beta > 0$ when β is such that $k_i = 0$ (we may also include the case $\partial k_r / \partial \beta < 0$ when β is such that $k_i = 0$, to be unstable, although there are no examples of this type of instability in our results). This then classifies all the supersonic modes as being stable, even though modes of $k_i \gtrless 0$ are found.

The inversion procedure outlined above leads to the following contribution to the perturbation wall shear for $X > 0$, namely

$$\bar{\tau}_{\text{discrete}} = \frac{e^{ik_0 X} f^*(k_0)\, \mathrm{Ai}\,(\zeta_0)\, k_0^2}{(ik_0)^{\frac{4}{3}}\left\{ -\dfrac{4}{3}\displaystyle\int_{\zeta_0}^{\infty} \mathrm{Ai}\,(\zeta)\, \mathrm{d}\zeta + \dfrac{2}{3}\left(\dfrac{\zeta_0^2}{k_0(ik_0)^{\frac{1}{3}}} - \zeta_0 \right) \mathrm{Ai}\,(\zeta_0) \right\}}, \qquad (2.22)$$

where k_0 is the root of (2.21) for the given value of β, and, if $\beta < \beta_c$, then k_0 lies in the third quadrant of complex-k-plane. Here we define

$$\zeta_0 = \frac{(ik_0)^{\frac{1}{3}}}{\beta^2 k_0}. \qquad (2.23)$$

Note that there can be no solution in the vicinity of the line $\arg(k) = -\frac{5}{4}\pi$ (unlike the supersonic case) since the left-hand side of (2.21) on this line is purely imaginary, whilst the right-hand side is purely real.

A further point of interest is the behaviour of k_0 as $\beta \to 0$. Using the asymptotic behaviour of Airy functions yields

$$k_0 \sim -\frac{1}{\beta} + \tfrac{1}{2}\beta\, e^{-\frac{1}{4}i\pi}. \qquad (2.24)$$

Consequently, as $\beta \to 0$ the curve in figure 2 approaches the negative real axis from below. In this limit the oscillations downstream grow more slowly (and have smaller wavelength), and so are generally of smaller amplitude. We expect the asymptotic results of I to hold upstream, and for $X < O(-1/\beta) \ln f^*(-1/\beta))$ downstream. This

requirement arises by demanding that the discrete contribution to the solution remains small.

Finally, the local maximum and minimum which are seen to occur in figure 2 at $\mathrm{Re}\,(k) \approx -3.5$ and $\mathrm{Re}\,(k) \approx -4$ respectively do appear to be genuine features of the curve.

We now go on to consider fully nonlinear solutions of (1.6); we shall be particularly interested in the effect of the nonlinearity on the waves predicted by linearized theory for the incompressible case.

3. Numerical scheme

We now consider a fully numerical approach to the solution of system (1.6)–(1.9). There are two main difficulties associated with the system (similar difficulties arise with the analogous steady problems). The first is the treatment of the pressure/displacement-function condition which demands, generally, an additional level of iteration in the computation. The incompressible condition (1.8) has been treated (in steady situations) by a number of authors, including Jobe & Burggraf (1974) in the context of trailing-edge flows and more recently by Veldman (1979) using a particularly efficient procedure. The supersonic condition (1.9) has also been treated by several workers in steady situations, for example Daniels (1974) (in the context of wake flows) using a method akin to a shooting technique. Rizzetta, Burggraf & Jenson (1978) developed a more reliable method that eliminated the need for this often troublesome and time-consuming procedure, but that still involved fairly lengthy computing times.

The second difficulty we incur will be our requirement for the correct treatment of reversing flow, if it occurs. Again, a number of numerical techniques are now available, but generally the solution procedure is further complicated. Possible schemes include those of Williams (1975) and of Rizzetta et al. (1978).

All the schemes mentioned above are based on adaptations of (now) fairly conventional finite-difference techniques. (In a recent paper by Smith 1984, which appeared during the course of preparation of this paper, there is a brief description of a finite-difference scheme to tackle unsteady problems of the present class using finite-difference techniques.) Instead we shall prefer to use an extension of a spectral method developed for steady flows by Burggraf & Duck (1981), and later used by Duck (1984) and Duck & Burggraf (1985). The idea behind this method stems from the linearized ($h \to 0$) treatment described in the previous section, the primary difference being that the $O(h^2)$ terms are retained (i.e. h is not assumed small), and the solution is then obtained through iteration. Much of the success of the method is undoubtedly a result of the previously discussed linearized solution giving remarkably good estimates for the nonlinear solution, even for $h = O(1)$. This technique, which is based on taking the Fourier transform of the equation in the streamwise direction, possesses two important advantages over more conventional finite-difference schemes. First, the method can incorporate any pressure/displacement relationship extremely easily and, secondly, it treats reversed-flow regions correctly, without the need for any kind of approximation or awkward adaptation as is required in conventional schemes. The scheme does have some drawbacks. For example it does not appear to be a simple matter to deal with mixed boundary conditions, such as encountered in trailing-edge regions. Further, difficulties can arise with discontinuous or unbounded wall distortions, since these can lead to singularities and slow decay in the (transformed) solution, which the scheme would have difficulty treating

accurately. However, since our main concern in this paper will be the effect of unsteadiness, rather than the detailed effects of surface geometry on the flow, we shall restrict our attention to smooth, bounded surface distortions, which result in flow disturbances which the transform method may treat relatively easily. We next describe the details of the procedure.

We differentiate (1.6) with respect to Y to obtain (2.1). Next we define a perturbation shear stress, this time given by

$$\tilde{\tau} = \Psi_{YY} - 1, \tag{3.1}$$

together with perturbation velocity components

$$\tilde{U} = \Psi_Y - Y, \tag{3.2}$$

$$\tilde{V} = -\Psi_X. \tag{3.3}$$

The system (2.1) may now be written in the form

$$\frac{1}{\beta^2}\tilde{\tau}_t + Y\tilde{\tau}_X - \tilde{\tau}_{YY} = -(\tilde{U}\tilde{\tau}_X + \tilde{V}\tilde{\tau}_Y). \tag{3.4}$$

For numerical expedience later, let us transform from the Y-coordinate, to the η-coordinate by means of

$$Y = f(\eta). \tag{3.5}$$

We shall restrict our attention to mappings that give

$$0 \leqslant Y < \infty \quad \text{as } 0 \leqslant \eta < 1. \tag{3.6}$$

This immediately implies one useful property, namely that the infinite-Y-domain is now reduced to a finite domain in η.

Substituting (3.5) into (3.4) gives

$$\frac{1}{\beta^2}\tilde{\tau}_t + f(\eta)\tilde{\tau}_X - \frac{1}{[f'(\eta)]^2}\tilde{\tau}_{\eta\eta} + \frac{f''(\eta)}{[f'(\eta)]^3}\tilde{\tau}_\eta = -\left(\tilde{U}\tilde{\tau}_X + \frac{\tilde{V}\tilde{\tau}_\eta}{f'(\eta)}\right) = R, \tag{3.7}$$

where we now have the following definitions

$$\left. \begin{array}{l} \tilde{\tau} = \dfrac{1}{[f'(\eta)]^2}\Psi_{\eta\eta} - \dfrac{f''(\eta)}{[f'(\eta)]^3}\Psi_\eta - 1, \\[3mm] \tilde{U} = \dfrac{1}{f'(\eta)}\Psi_\eta - f(\eta). \end{array} \right\} \tag{3.8}$$

The next step is to Fourier transform (3.7) with respect to X, yielding

$$\frac{1}{\beta^2}\tilde{\tau}_t^* + \mathrm{i}kf(\eta)\tilde{\tau}^* - \frac{1}{[f'(\eta)]^2}\tilde{\tau}_{\eta\eta}^* + \frac{f''(\eta)}{[f'(\eta)]^3}\tilde{\tau}_\eta^* = -\left(\tilde{U}\tilde{\tau}_X + \frac{\tilde{V}\tilde{\tau}_\eta}{f'(\eta)}\right)^* \tag{3.9}$$

$$= R^*(k, \eta, t). \tag{3.10}$$

Here an asterisk again denotes a transform variable, for example

$$\tilde{\tau}^*(k, \eta, t) = \int_{-\infty}^{\infty} \tilde{\tau}(X, \eta, t)\,\mathrm{e}^{-\mathrm{i}kX}\,\mathrm{d}X. \tag{3.11}$$

The boundary conditions to be applied to (3.10) are that

$$\tilde{V}^*(\eta = 0) = \tilde{U}^*(\eta = 0) = 0 \tag{3.12}$$

together with $$\tilde{\tau}^* \to 0 \quad \text{as} \quad \eta \to 1. \tag{3.13}$$

Notice that (for the purposes of the right-hand side of (3.10))

$$\left. \begin{aligned} \tilde{U}^* &= \int_0^\eta f'(\eta_1)\,\tilde{\tau}^*(\eta_1)\,\mathrm{d}\eta_1, \\ V^* &= -\mathrm{i}k \int_0^\eta f'(\eta_2) \int_0^{\eta_2} f'(\eta_1)\,\tilde{\tau}^*(\eta_1)\,\mathrm{d}\eta_1\,\mathrm{d}\eta_2. \end{aligned} \right\} \tag{3.14}$$

We still require to implement (1.7b) as $\eta \to 1$, together with the appropriate pressure/displacement relationship, either (1.8) or (1.9). Suppose that the Fourier transform of this may again be written as

$$P^* = \Lambda(k)\,A^*, \tag{3.15}$$

then
$$\Lambda(k) = -\mathrm{i}k \quad \text{for supersonic flows,} \tag{3.16}$$

whilst
$$\Lambda(k) = (k^2)^{\frac{1}{2}} \quad \text{for incompressible flows.} \tag{3.17}$$

From (1.7b) we find that, as $\eta \to 1$,

$$\int_0^\eta f'(\eta)\,\tilde{\tau}^*(\eta)\,\mathrm{d}\eta \to A^* + hF^*. \tag{3.18}$$

We still require one further condition to enable us to eliminate the pressure. This is derived from evaluating (1.6) on $Y = 0$, and using the wall boundary conditions, to give

$$\left. \frac{\tilde{\tau}_\eta^*}{f'(\eta)} \right|_{\eta=0} = \mathrm{i}kP^*. \tag{3.19}$$

Combining (3.15), (3.18) and (3.19) results in a final condition

$$\left. \frac{\tilde{\tau}_\eta^*}{f'(\eta)} \right|_{\eta=0} = \mathrm{i}k\Lambda \left\{ \left[\int_0^\eta f'(\eta)\,\tau^*\,\mathrm{d}\eta \right]_{\eta \to 1} - hF^* \right\}. \tag{3.20}$$

We now seek a numerical solution to (3.10), subject to (3.13) and (3.20). We shall solve for $\tilde{\tau}^*$, at times given by $t = (i-1)\Delta t$ $(i = 1, 2, \ldots)$, at J η-stations given by $\eta = (j-1)\Delta\eta$, such that $\Delta\eta = \eta_\infty/(J-1)$, $1-\eta_\infty \ll 1$, $j = 1, 2, \ldots$ at K k-points in the range $k_{\min} \leqslant k \leqslant k_{\max}$. The solution procedure is similar to that of Burggraf & Duck (1981) and Duck (1984) (although these authors considered steady problems, and also did not use the transformation (3.5)).

At each $(k, \eta, t-\frac{1}{2}\Delta t)$-station, (3.10) is approximated by

$$\frac{1}{\Delta t\,\beta^2}\left[\tilde{\tau}^*(k, \eta, t) - \tilde{\tau}^*(k, \eta, t-\Delta t)\right]$$

$$+ \tfrac{1}{2}\mathrm{i}kf(\eta)[\tilde{\tau}^*(k, \eta, t) + \tilde{\tau}^*(k, \eta, t-\Delta t)]$$

$$- \frac{1}{2(\Delta\eta)^2\,[f'(\eta)]^2}\{\tilde{\tau}^*(k, \eta+\Delta\eta, t) - 2\tilde{\tau}^*(k, \eta, t) + \tilde{\tau}^*(k, \eta-\Delta\eta, t)$$

$$+ \tilde{\tau}^*(k, \eta+\Delta\eta, t-\Delta t) - 2\tilde{\tau}^*(k, \eta, t-\Delta t) + \tilde{\tau}^*(k, \eta-\Delta\eta, t-\Delta t)\}$$

$$+ \frac{f''(\eta)}{4\Delta\eta[f'(\eta)]^3}\{\tilde{\tau}^*(k, \eta+\Delta\eta, t) - \tilde{\tau}^*(k, \eta-\Delta\eta, t)$$

$$+ \tilde{\tau}^*(k, \eta+\Delta\eta, t-\Delta t) + \tilde{\tau}^*(k, \eta-\Delta\eta, t-\Delta t)\} = R^*(k, \eta, t-\tfrac{1}{2}\Delta t), \quad (3.21)$$

for $\Delta\eta \leqslant \eta \leqslant \eta_\infty - \Delta\eta$. Notice the error of this scheme is $O((\Delta t)^2 + (\Delta\eta)^2)$.

The condition (3.20) was approximated using second-order (three-point backward) differencing for the derivative of $\tilde{\tau}^*$, and trapezoidal quadrature for the integral.

Notice that, although $f'(\eta)$ becomes algebraically large as $\eta \to 1$, $\tilde{\tau}^*$ decays exponentially in this limit, and so the integrand in (3.20) decays as $\eta \to 1$. Equation (3.20) was evaluated at time t, rather than at time $t - \frac{1}{2}\Delta t$ as was used for (3.10).

At each (k, t)-station with $\Delta \eta \leqslant \eta \leqslant \eta_\infty - \Delta \eta$, we have a tridiagonal system to solve, but with a full bottom row corresponding to (3.20). Gaussian elimination may be employed to solve for each $\tilde{\tau}(\eta)$. Notice one extremely useful property, namely

$$\tilde{\tau}^*(-k, \eta, t) = \text{complex-conjugate } \{\tilde{\tau}^*(k, \eta, t)\}, \tag{3.22}$$

a result which enables us to halve the amount of computing required. We chose to consider just $k \leqslant 0$.

The overall procedure was then as follows: using the values of $\tilde{\tau}^*$ at the previous timestep, the right-hand side of (3.21) was evaluated at all (k, η)-stations by inverting $\tilde{\tau}^*$ and $ik\tilde{\tau}^*$ and using the fast-Fourier-transform method of Cooley & Tukey (1965), to yield the physical variables $\bar{U}, \tilde{\tau}_X, \bar{V}, \tilde{\tau}_\eta$. $R(X, \eta, t)$ was then evaluated in physical space, before transforming back into transform space, again by means of the fast-Fourier-transform technique. This system for evaluating the right-hand side of (3.21), although appearing to be rather cumbersome, was used in preference to evaluation of a convolution integral, which in fact involves considerably more operations than our method. The system was then solved by sweeping through all the k-stations (solving along lines of $k = $ constant), and the right-hand side was then re-evaluated using the method outlined above. The process was then repeated until convergence. This was taken to be when the maximum change in any of the pressures (obtained using (3.19)) was less than 10^{-7}. Once convergence was achieved, the calculation was carried on to the next timestep, and the overall procedure repeated. Note that, at the very first timestep, for the first iteration we set $R(k, \eta, 0) = 0$ for all k, η. Once convergence had been achieved the results were finally inverted by means of trapezoidal quadrature.

The particular version of the fast Fourier transform used required a slight bias in k, namely $k_{\max} = -k_{\min} - \Delta k$, and we assumed values for $k > k_{\max}$ to be equal to values for $k < k_{\min}$, namely zero. However the errors involved with this are expected to be insignificant, owing to the generally rapid decay of the transformed solution as $|k| \to \infty$. A further point is that the range in k may be interpreted as a (physical) range in X, namely

$$-\tfrac{1}{2}(K+1)\Delta X < X < \tfrac{1}{2}(K+1)\Delta X, \tag{3.23}$$

as $k_{\min} < k < -k_{\min} - \Delta k$, assuming K is even, and where

$$\Delta k = -\frac{2k_{\min}}{K-1}, \quad \Delta X = \frac{2\pi}{K\Delta k}. \tag{3.24}$$

A much fuller account of these and related matters is given by Burggraf & Duck (1981).

4. Results

Generally, we chose

$$f(\eta) = \frac{\eta}{1 - \eta}, \tag{4.1}$$

with $0 \leqslant \eta \leqslant 0.95$. It was found that this transformation gave considerably more accurate results for the same number of points than control computations carried out using an untransformed (i.e. $f(\eta) = \eta$) grid.

Further, we generally took the following perturbation shape

$$F(X,t) = \begin{cases} 0, & t < 0, \\ \dfrac{\sin t}{1 + X^2}, & t > 0, \end{cases} \tag{4.2}$$

corresponding to an impulsively started distortion. Note that the Fourier transform (with respect to X) of this $F(X,t)$ is

$$F^*(k,t) = \begin{cases} 0, & t < 0, \\ \pi\,\mathrm{e}^{-|k|}\sin t, & t > 0 \end{cases} \tag{4.3}$$

(assuming k to be real).

This impulsive start to the movement of the distortion does induce a singular behaviour in the solution for small t, and results in a thin boundary layer of thickness $O(t^{\frac{1}{2}})$. However, during this phase of the motion the streamwise perturbation velocity is generally $O(t^2)$, and consequently this singular start-up process was found to have little effect on the accuracy of results at later times. (It would be possible to incorporate this singular behaviour into a numerical scheme; although routine, it would complicate our method further.)

4.1. *Supersonic case*

Figure 3 (a, b) shows the perturbation wall shears $(\tilde{\tau}_{\mathrm{w}})$ and the perturbation pressure distributions for the example $h = \beta = 1$. The solid curve represents nonlinear results obtained with the following grid:

$$k_{\min} = -14.11, \quad k_{\max} = 13.89, \quad K = 256,$$

with

$$J = 25, \quad \text{and} \quad \Delta t = 0.005.$$

We shall refer to this as grid I. This particular computation took approximately $1\frac{1}{2}$ hours of CDC 7600 time in order to reach $t = 3\pi$. These results were checked by a control computation carried out on a coarser, less-extensive grid, namely $k_{\min} = -7.22$, $k_{\max} = 6.88$, $K = 64$, $J = 25$, $\Delta t = 0.005$. We shall refer to this as grid II. For the example shown in figure 3 (a, b), the results obtained on grids I and II were identical to within 1 % and were indistinguishable graphically (a certain amount of numerical experimentation with J was also carried out, and it was deemed that $J = 25$ gave similar accuracy). In order to gauge the amount of nonlinearity in the solution, the linearized solution was generated on grid II, by setting $R^* = 0$ at all points, for all times. Note that no iteration is necessary for these linearized results. Discrepancies only between the linear and nonlinear solutions are shown, this discrepancy being indicated by the broken lines on figure 3 (a, b). The linear solution is only shown at $t = \frac{5}{2}\pi$ and $t = 3\pi$, since, to 2 places of decimals we found that by $t = \frac{3}{2}\pi$ we had already obtained

$$P(t+\pi) = -P(t), \quad \tilde{\tau}_{\mathrm{w}}(t+\pi) = -\tilde{\tau}_{\mathrm{w}}(t), \tag{4.4}$$

indicating that the transient part of the solution, due to the impulsive start, decays very rapidly with t.

The second example shown is a rather more challenging case of $h = 5$, $\beta = 1$ (a somewhat larger wall perturbation); these results are shown in figure 4 (a, b), and were produced using the (coarse) grid II. Notice, in particular, how at $t = \frac{3}{2}\pi$ there appears to be a pressure plateau developing in the region of reversed flow $(\tilde{\tau} < -1)$, a
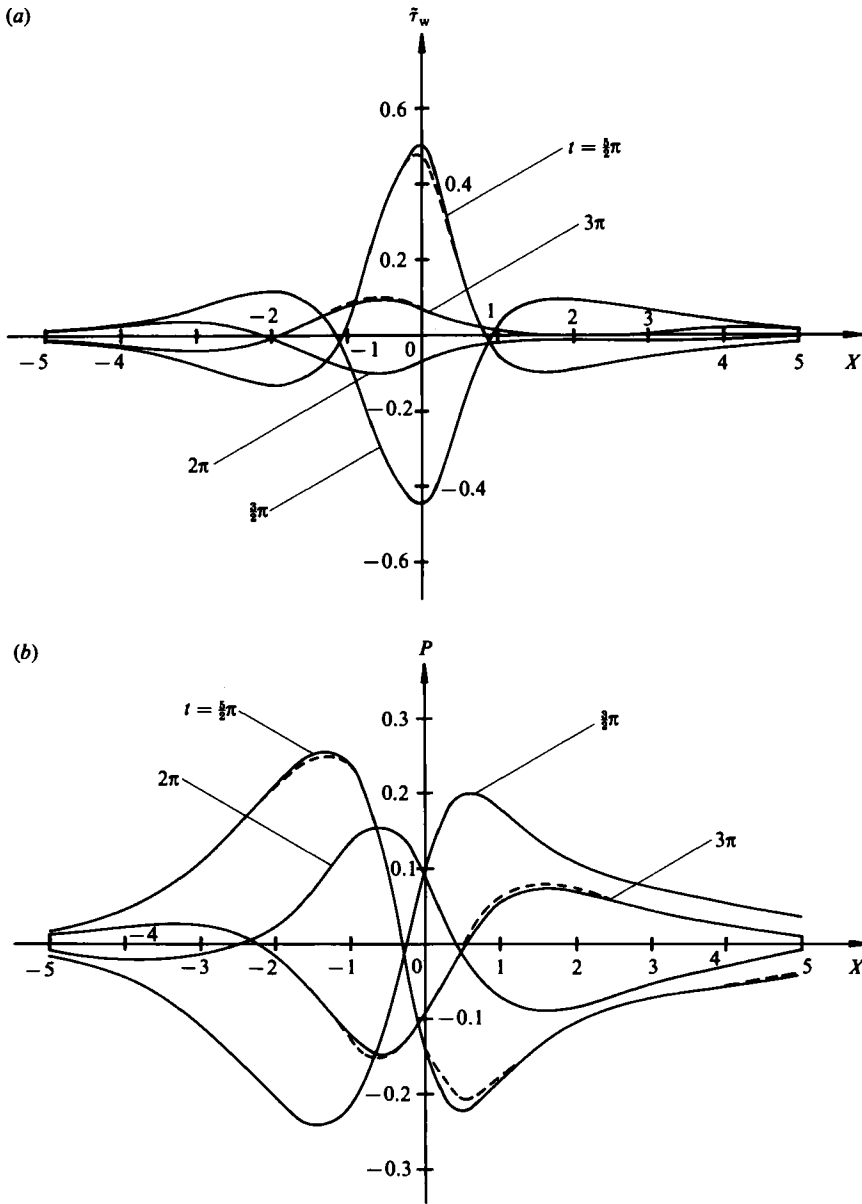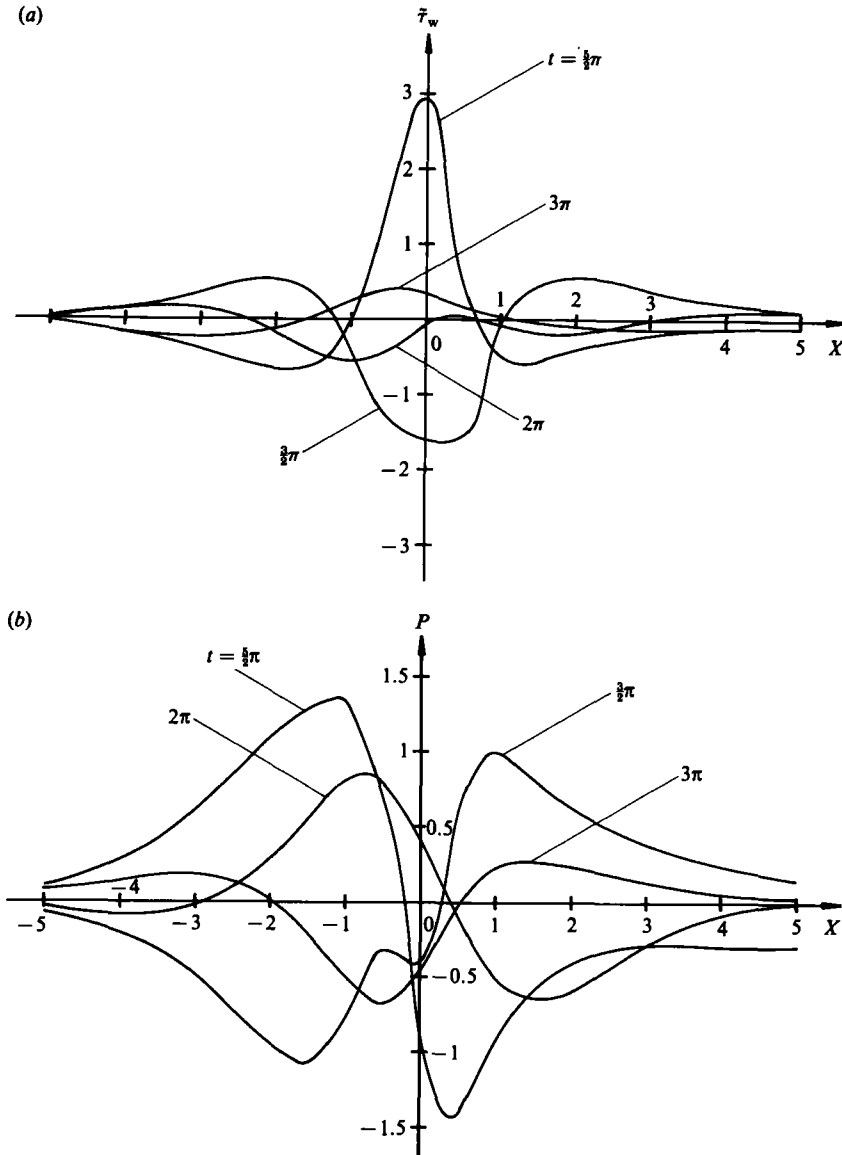
FIGURE 3. (a) Spatial distribution of perturbation wall shear; (b) spatial distribution of perturbation pressure: $h = \beta = 1$, supersonic case.

phenomenon observed with steady flows with large separated regions. It appears that the reversal of the flow occurs quite regularly here. A further feature observed in figure 4(a), which is commonly observed in steady flows of this class, is that the effect of the nonlinearity is to reduce the magnitude of the reversed flow, compared with that which might be expected to occur from the linearized $\tilde{\tau}_w$ distribution (see figure 3a).

The next example tackled was $h = 7.5$, $\beta = 1$. Results for the perturbation wall shear for this case are shown in figure 5(a, b), at six different times. These results

(a)

(b)

FIGURE 4. (a) Spatial distribution of perturbation wall shear; (b) spatial distribution of perturbation pressure: $h = 5$, $\beta = 1$, supersonic case.

we computed on a third grid, grid III, with $k_{\min} = -14.22$, $k_{\max} = 13.88$, $K = 128$, $J = 25$, $\Delta t = 0.005$. These results illustrate a feature not readily observable in any of the previous sets of results. After $t \doteq 4$, the shear distributions are beginning to exhibit a progressively severe minimum, up to $t \doteq 5$. Thereafter this minimum decreases very rapidly in magnitude, and is swept downstream as a decreasing-amplitude wave. The behaviour of the transformed (i.e. Fourier) variables (which are not illustrated) is also interesting around $t = 5$. The decay as $k \to -\infty$ became progressively slower, and then, as the shear minimum subsided, the decay improved drastically. The results for all the other variables exhibited a similar type of behaviour.
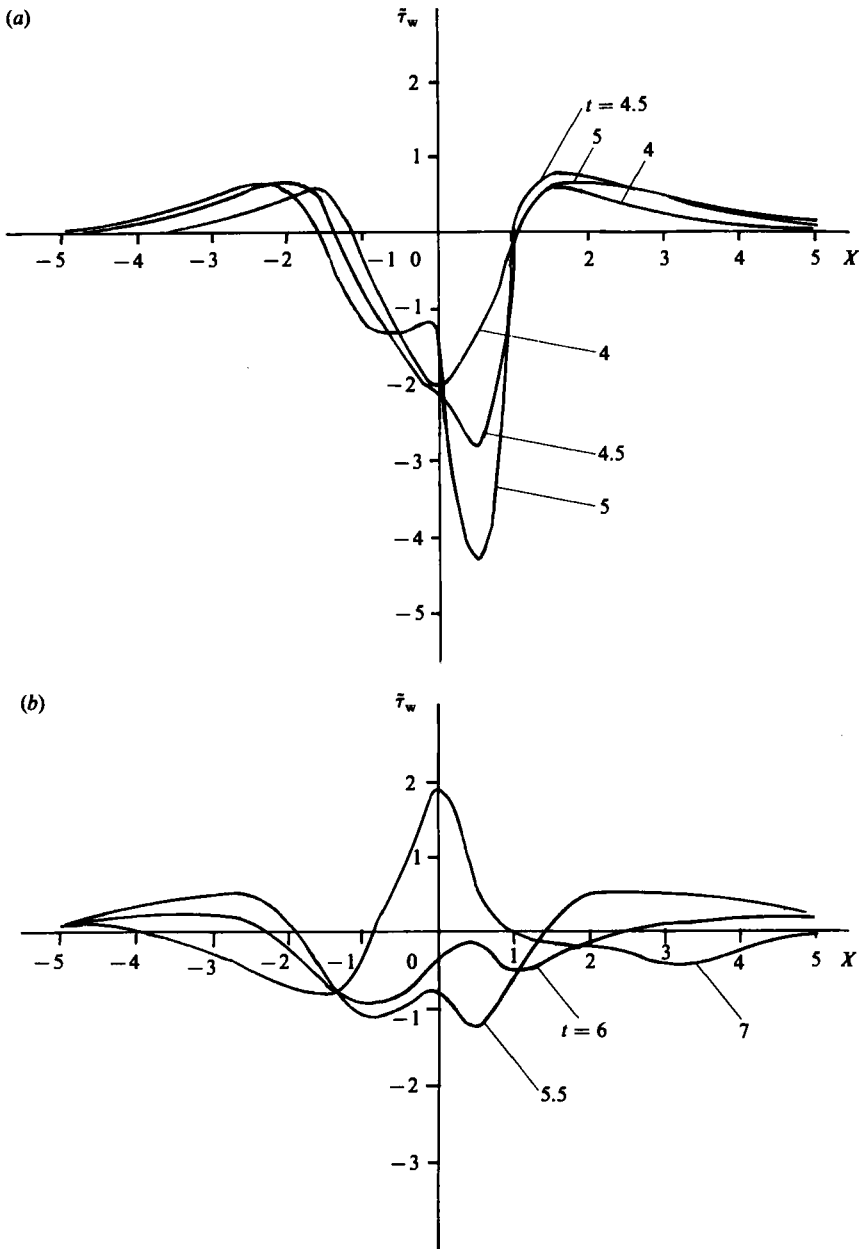
FIGURE 5(a, b) Spatial distribution of perturbation wall shear, $h = 7.5$, $\beta = 1$, supersonic case.

The most severe height tackled was $h = 10$ (with $\beta = 1$, still). Results for the perturbation wall shear, obtained on grid III, are shown in figure 6. Up to $t \doteq 2.50$ no particularly unexpected phenomena occur. At $t = 2.75$ several (mild) oscillations begin, and, by $t = 2.875$, these have grown into quite severe oscillations. Associated with this behaviour, the Fourier variables were seen to no longer decay as $k \to -\infty$. As a result the computation became extremely sensitive to the choice of the range of k (a control calculation using grid II was also performed). This type of apparent breakdown of the governing equations (which may involve a corresponding breakaway
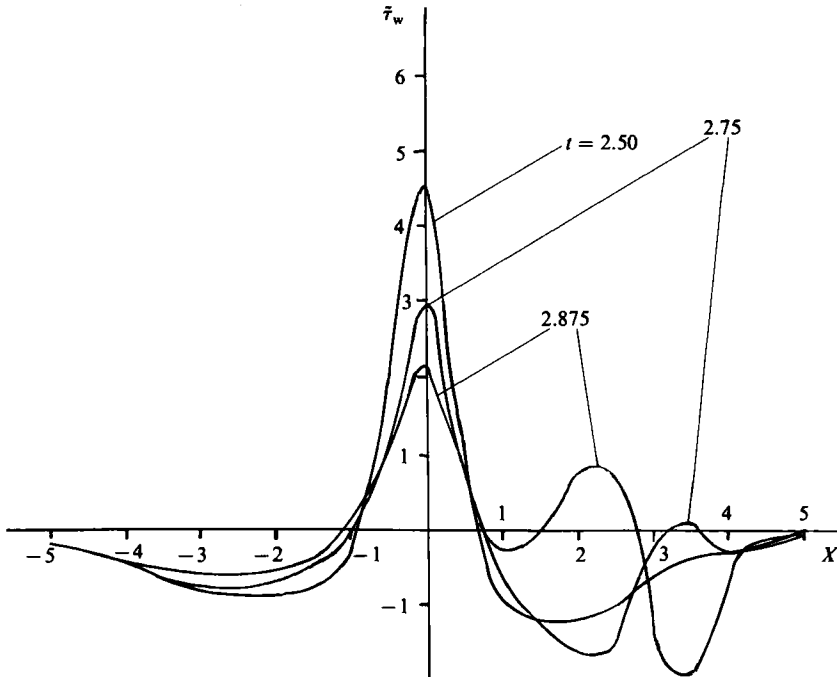
FIGURE 6. Spatial distribution of perturbation wall shear, $h = 10$, $\beta = 1$, supersonic case.

of a free shear layer) has been found in other unsteady situations by Duck (1985) in pulsatile internal flows, and by Tutty & Cowley (1985). Unlike the present problem, in both these papers the situation was slightly simpler, being 'non-interacting', i.e. with $A \equiv 0$. The latter authors also conjectured that the genesis of the breakdown was a short-wavelength (i.e. $|k| \gg 1$) Rayleigh-type instability, associated with inflection-type profiles, and our results (in k-space) do indeed point to a very rapid growth rate as $k \to -\infty$, at certain times throughout the cycle.

Our computation for $h = 10$ in fact continued (confirming the robust nature of the numerical scheme), up to $t \doteq 4.75$, when it eventually failed to converge within a specified number of iterations. After $t = 3$ the oscillations in the distributions began to decrease in amplitude (this was accompanied by a restoration of decay of Fourier variables for large $-k$), and were swept downstream (although, after $t = 3$, the accuracy of the results is open to question). After $t \doteq 4.25$ a very sharp minimum in wall shear distribution began to develop quickly, associated with a further lack of decay of the Fourier variables as $k \to -\infty$. In general there seem to be two 'danger periods' when breakdown is likely. For $h = 10$, the first occurs around $t = 3$ and is the less 'dangerous' (our $h = 7.5$ results showed little sign of any breakdown/oscillation around this time). The second 'danger period' is close to $t = 4.5$. This type of behaviour is clearly a nonlinear phenomenon, and cannot be described by the linearized theory of the previous section.

The final supersonic example tackled was $h = 1$, $\beta = \frac{1}{4}$, using grid II. This corresponds to a rather faster wall oscillation than the previous examples. The results, shown in figure 7 (a, b), indicate that the perturbation-wall-shear distributions are almost symmetrical about $X = 0$, whilst the pressure distributions are practically antisymmetric about $X = 0$. These observations may be explained using I (although I was concerned primarily with incompressible flows, it is a trivial matter to extend
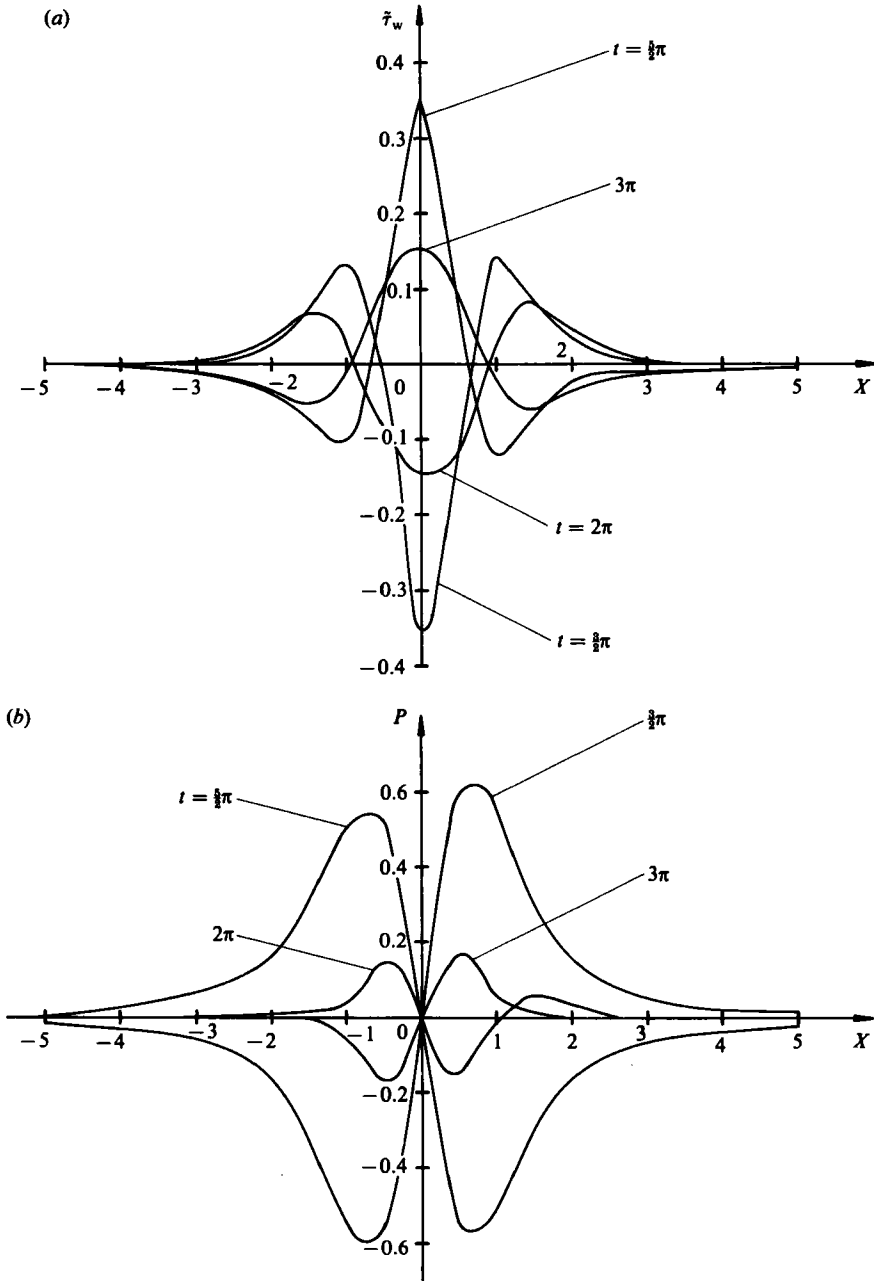
FIGURE 7. (a) Spatial distribution of perturbation wall shear; (b) spatial distribution of perturbation pressure: $h = 1$, $\beta = \frac{1}{4}$, supersonic case.

these results to supersonic flows, simply by replacing (1.8) with (1.9)). This yields, as $\beta \to 0$ (assuming the transient solution has decayed)

$$\left. \begin{array}{l} P = hF_X + O(\beta^2), \\ \tilde{\tau}_w = \{ -h\beta f_{XX}\, \mathrm{e}^{\mathrm{i}(t-\frac{1}{4}\pi)} + \text{c.c.} \} + O(\beta^3), \end{array} \right\} \tag{4.5}$$

where

$$F(X, t) = f(X)\, \mathrm{e}^{\mathrm{i}t} + \text{c.c.},$$

and 'c.c.' denotes a complex conjugate. For the particular example of (4.2), these give

$$P = \frac{-2hX}{(1+X^2)^2} \sin t + O(\beta^2), \tag{4.6}$$

$$\tilde{\tau}_w = h\beta \cos(t + \tfrac{1}{4}\pi) \left\{ \frac{-2}{(1+X^2)^2} + \frac{8X^2}{(1+X^2)^3} \right\} + O(\beta^3). \tag{4.7}$$

Comparison of the computed pressure distribution with (4.6) shows good agreement. The agreement between the computed and asymptotic wall shears is less good, although if we compare figure 3(a) with figure 7(a), then there is a definite trend towards (4.7). This slower approach of the shear towards its asymptotic value is caused, presumably, because (4.7) is a second-order ($O(\beta)$) term, whilst (4.6) represents a leading-order ($O(1)$) term.

4.2. *Incompressible case*

The first incompressible example tackled was for $h = \beta = 1$. First the (fine) grid I was used. However the computation failed to converge at $t \approx 5$, and the calculation was then halted. Figure 8(a, b) shows (solid lines) perturbation wall shear and pressure distributions at three times before this failure occurred. The solution showed no real signs of problems just prior to failure, except for a number of mild spatial and temporal 'ripples' for $|X|$ large. A second computation was then carried out using the coarser grid II. At $t = \tfrac{1}{2}\pi$ there was agreement to within 1 % of the grid I results; at $t = \pi$, the agreement was less satisfactory, with the grid II solution developing some moderate oscillations for $|X| \gg 1$; at $t = \tfrac{3}{2}\pi$ this (grid II) solution exhibited general large-scale oscillations, and the computation ultimately failed at $t \doteq 5$ (again). This type of behaviour strongly suggested that numerical difficulties were being encountered (dependent partly on mesh size). The nature of this failure was quite different from that observed in the large-h supersonic examples, in which oscillations and rapid solution growth occurred over a more localized region.

At first it was thought that these difficulties might be associated with the fast-Fourier-transform routine, and so next the linearized solution was generated using both grids. The departure of these grid I results from the nonlinear solution is shown as broken lines on figure 8(a,b). Again, with grid I after $t \doteq \tfrac{3}{2}\pi$ spatial and temporal oscillations started to occur for $|X| \gg 1$, initially very mild in nature, but increasing in magnitude with time. Using the coarse grid II, oscillations started to occur at $t \doteq 2$ (much earlier than on grid I), which again increased in strength with time. These results thus eliminated the possibility that the difficulties were caused (directly) by the fast-Fourier-transform routine, and so we must find an alternative explanation for these difficulties.

In an attempt to gauge the effect of the start-up process on the solution, we next considered the following distortion:

$$F(X, t) = \begin{cases} 0, & t < 0, \\[2mm] \dfrac{\sin(t)}{1+X^2}, & 0 < t < \tfrac{1}{2}\pi, \\[3mm] \dfrac{1}{1+X^2}, & t > \tfrac{1}{2}\pi, \end{cases} \tag{4.8}$$
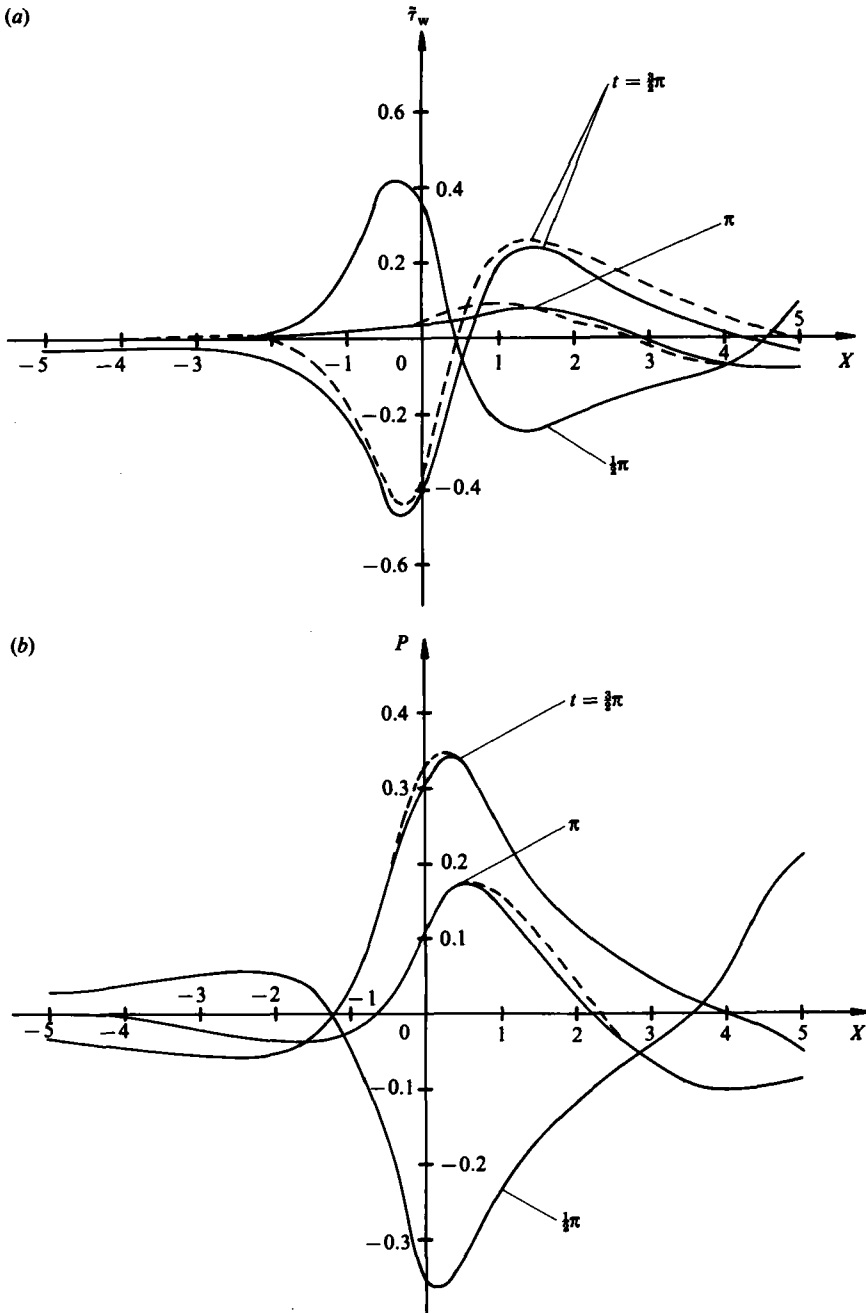
FIGURE 8. (a) Spatial distribution of perturbation wall shear; (b) spatial distribution of perturbation pressure: $h = \beta = 1$, incompressible case.

with again $h = \beta = 1$. As $t \to \infty$, the solution should approach the steady state. Grid I was used to compute both the nonlinear and linear solutions, and figure 9 shows the time variation of the perturbation wall shear, at specified X stations, for the nonlinear case (the linearized results were very similar). It is apparent that, even though $\beta > \beta_c$, the start-up process is triggering unstable modes, which give rise to
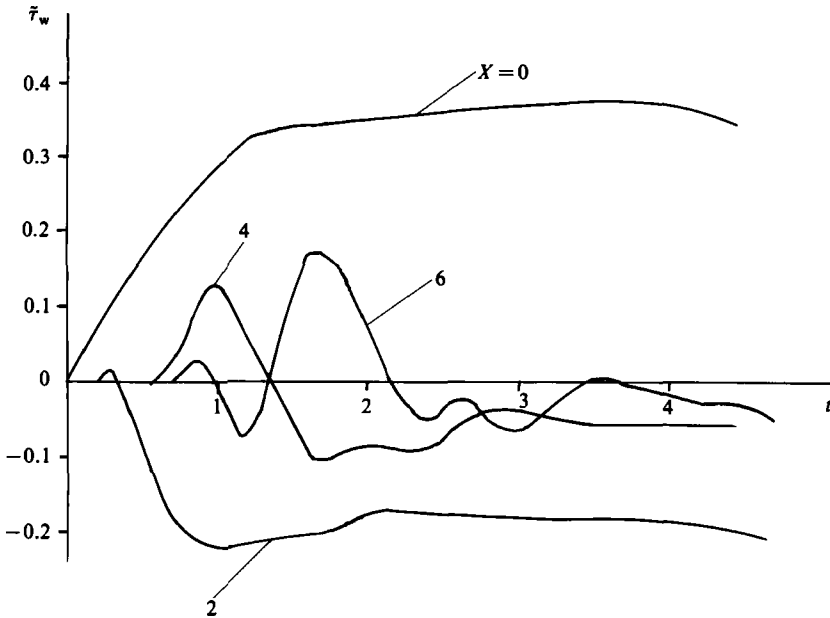
FIGURE 9. Time variation of perturbation wall shear $h = \beta = 1$
(distortion 4.8, nonlinear results).

downstream-growing waves. This feature was common to both the linear and nonlinear cases (we shall later see an additional mechanism in the nonlinear case that can also trigger unstable modes). However, for fixed X, these waves do become smaller in amplitude with time, indicating the eventual formation of the steady state. As might be expected, the further downstream the station, the slower this approach to the steady state. This nonlinear computation (also) failed at $t \doteq 5$ in a manner similar to that for the sinusoidally time-varying distortion. Consequently we conclude that this failure of the scheme is related to the start-up process, which triggers all (time) modes, in addition to that mode corresponding to the hump oscillation.

It is interesting to observe the nature of the transformed solution; in figure $10(a, b)$ the distributions of Re $(-A^*)$ at $t = 4.57$ are shown for the nonlinear and linear calculations respectively. These distributions are typical of all transformed quantities at this (and neighbouring) timesteps. Particularly noticeable (in both cases) are the extremely rapid and large oscillations of the distributions. Comparing the nonlinear to the linear results, from $k = 0$ up to $k \doteq -3.25$, the two sets are very similar; in both cases the maximum amplitude is attained at around $k = -2.5$, this being in agreement with figure 2, which suggests that the maximum growth rate for the linearized case, corresponding to the minimum of Im (k), will also occur at $k \doteq -2.5$ (a measure of the decay/growth of disturbances is given by the distance of the roots on figures 1 and 2 from the real axis – the greater this distance, the greater the decay/growth rate).

Further understanding of the start-up process may be obtained from studying the linearized problem, using essentially the same techniques as in §2, except here we consider more general time variations of $F(X, t)$ (including impulsively started forms), rather than purely oscillatory forms. To do this we first take the double Fourier
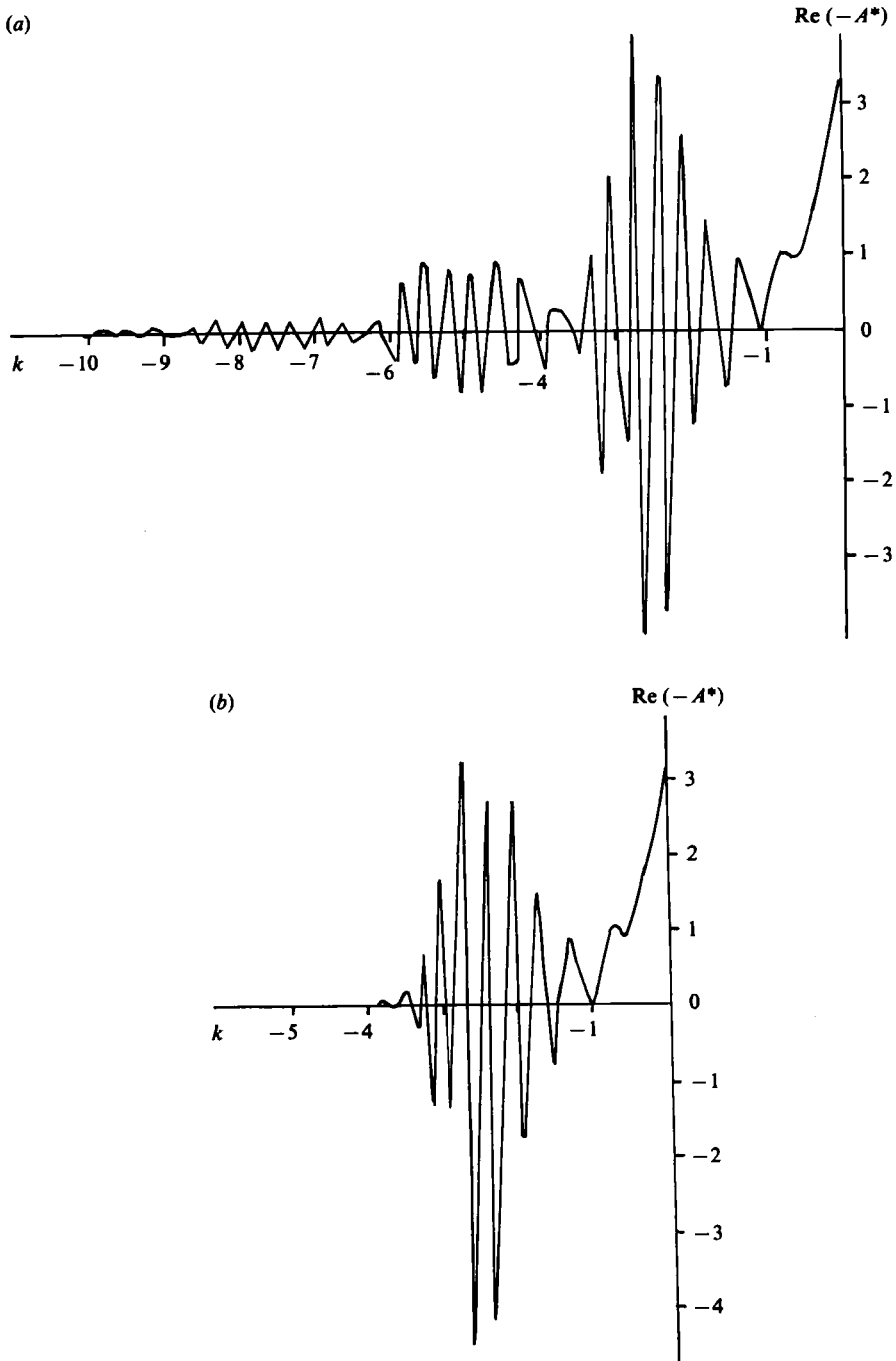
(a)

(b)

FIGURE 10. Re($-A^*$) distribution, $h = \beta = 1$, distortion (4.8), $t = 4.57$. (a) nonlinear case, (b) linearized case.
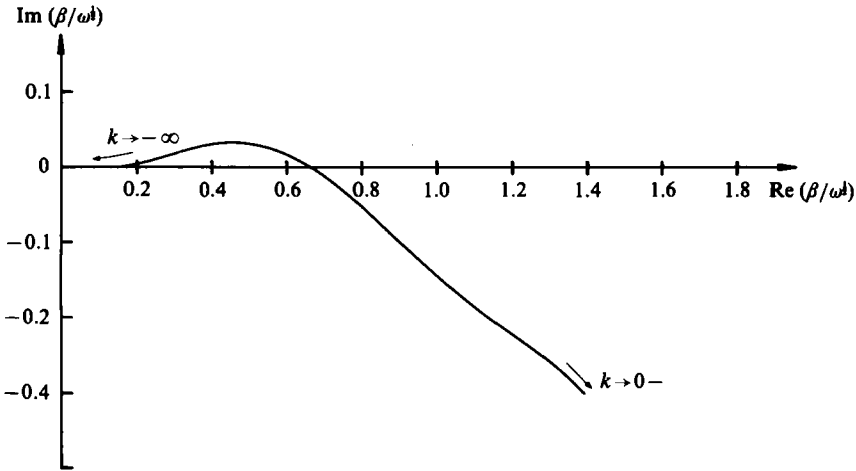
FIGURE 11. Roots of (4.13), k prescribed, incompressible case.

transform of (2.2), where

$$f^{**}(k,\omega) = \int_{-\infty}^{\infty} \int_{-\infty}^{\infty} F(X,t)\,e^{-ikX-i\omega t}\,dt\,dX, \tag{4.9}$$

$$\tilde{\tau}^{**} = \int_{-\infty}^{\infty} \int_{-\infty}^{\infty} \tilde{\tau}(X,Y,t)\,e^{-ikX-i\omega t}\,dt\,dX, \tag{4.10}$$

giving the following equation for $\tilde{\tau}^{**}$:

$$\frac{i\omega}{\beta^2}\tilde{\tau}^{**} + ik\,Y\tilde{\tau}^{**} - \tilde{\tau}^{**}_{YY} = 0. \tag{4.11}$$

The solution of this may be simply inferred from (2.7), giving

$$\tilde{\tau}^{**} = \frac{ik(k^2)^{\frac{1}{2}}hf^{**}(k,\omega)\,\mathrm{Ai}\left\{(ik)^{\frac{1}{3}}\left(Y+\dfrac{\omega}{k\beta^2}\right)\right\}}{(ik)^{\frac{2}{3}}(k^2)^{\frac{1}{2}}\displaystyle\int_{\omega(ik)^{\frac{1}{3}}/\beta^2 k}^{\infty}\mathrm{Ai}\,(\zeta)\,d\zeta - (ik)^{\frac{1}{3}}\,\mathrm{Ai}\left[\dfrac{\omega(ik)^{\frac{1}{3}}}{\beta^2 k}\right]}. \tag{4.12}$$

We now consider the locations of poles of this expression, namely roots of the equation

$$(ik)^{\frac{1}{3}}(k^2)^{\frac{1}{2}}\int_{\omega(ik)^{\frac{1}{3}}/\beta^2 k}^{\infty}\mathrm{Ai}\,(\zeta)\,d\zeta = \mathrm{Ai}'\left[\frac{\omega(ik)^{\frac{1}{3}}}{\beta^2 k}\right]. \tag{4.13}$$

However, this time we take a slightly different approach to the problem from that used before, namely: given a value of k (real), what is the corresponding value(s) of ω/β^2? We may allow ω/β^2 to be complex. The variation of the roots of (4.13) is shown in figure 11. For each value of k (negative and real) there appears to be just one value of ω/β^2. The crucial point is again the cross-over of the real axis. Indeed, from figure 2 we may have inferred that this would occur, at $\omega/\beta^2 = 1/\beta_c^2$, $k = k_c$. We now invoke similar arguments to those used earlier, in the inversion of (for example) $\tilde{\tau}^{**}(k,Y,\omega)$, to obtain $\tilde{\tau}^*(k,Y,t)$ (this being the quantity computed in the numerical method). For $t < 0$, we must have a trivial solution for all perturbation quantities, assuming the distortion is introduced at $t = 0$. For $t > 0$ we would ordinarily expect to take a contour lying completely within the upper half-plane of the complex-ω-plane.

However, we see that, for $k < k_c$, the root $\omega_0(k)$ is such that $\mathrm{Im}\{\beta/\omega_0^{\frac{1}{2}}\} > 0$, implying $\mathrm{Im}\,[\omega_0] < 0$, and so the inversion contour must be diverted into the lower half of the complex-ω-plane to include the corresponding pole at $\omega = \omega_0$. Thus at each value of k, $k < k_c$, $\tilde\tau^*$ includes a factor $\mathrm{e}^{\mathrm{i}\omega_0(k)\,t}$, such that $\mathrm{Im}\{\omega_0\} < 0$. Further, since it is $\Omega_0 = \omega_0/\beta^2$ that is the important dependent variable, more specifically we may write the discrete contribution to the perturbation wall shear $\tilde\tau^*_{\mathrm{w}}$ symbolically as

$$\tau^*_{\mathrm{w}} = H(k)\,\mathrm{e}^{\mathrm{i}\Omega_0(k)\,\beta^2 t}, \tag{4.14}$$

where we suppose

$$\Omega_0(k) = \Omega_{\mathrm{r}}(k) - \mathrm{i}\Omega_{\mathrm{i}}(k), \tag{4.15}$$

such that

$$\Omega_{\mathrm{i}}(k) > 0 \quad \text{for } |k_c| < |k| < \infty. \tag{4.16}$$

We then have that

$$\tilde\tau_{\mathrm{discrete}} = \frac{1}{\pi}\,\mathrm{Re}\!\left[\int_{-\infty}^{k_c} H(k)\,\mathrm{e}^{\mathrm{i}\Omega_0(k)\,\beta^2 t + \mathrm{i}kX}\,\mathrm{d}k\right] \tag{4.17}$$

is the growing contribution to the (physical) quantity $\tilde\tau_{\mathrm{w}}$. As $t \to -\infty$, $-\infty < k < k_c$, (4.14) grows (exponentially) and also oscillates increasingly rapidly. To determine an asymptotic estimate for (4.17) we write

$$\tilde\tau_{\mathrm{discrete}} = \frac{1}{\pi}\,\mathrm{Re}\!\left[\int_{-\infty}^{k_c} G(k)\,\Omega'_0(k)\,\mathrm{e}^{\mathrm{i}\Omega_0(k)\,\beta^2 t + \mathrm{i}kX}\,\mathrm{d}k\right], \tag{4.18}$$

where $G(k) = H(k)/\Omega'_0(k)$. Here we expect $\Omega'_0(k)$ to be a complex monotonic function of k, $-\infty < k < k_c$. Integrating (4.18) once by parts, we obtain

$$\tilde\tau_{\mathrm{discrete}} \sim \frac{1}{\pi}\,\mathrm{Re}\!\left[\mathrm{i}\,\frac{G(k_c)}{\beta^2 t}\,\mathrm{e}^{\mathrm{i}\Omega_{\mathrm{r}}(k_c)\,\beta^2 t + \mathrm{i}k_c X}\right] + O(t^{-2}) \tag{4.19}$$

provided

$$|\Omega_{\mathrm{r}}(k_c)\,\beta^2 t| \gg |k_c X|. \tag{4.20}$$

Equation (4.19) indicates that, for fixed X, the transient solution, which causes numerical difficulties, decays with time (at least in the linearized case). When $\Omega_{\mathrm{r}}(k_c)\,\beta^2 t = -k_c X$ then we obtain the (increasing-amplitude) wave packet as seen in figure 9 (the position of the wave being in fair agreement with this expression).

Thus in spite of the increasingly large and rapid oscillations of the solution in k-space, the physical solution is generally well behaved, except near the wave packet, which is propagated downstream. However a stage is reached (dependent on the spacing of the k-points), where the quadrature scheme used to invert the transformed solution is unable to treat these oscillations accurately, and this eventually results in the erroneous oscillations in our physical solutions. Because of the multiplicative β^2 in the exponential term of (4.18) as $\beta \to 0$, these difficulties are likely to develop more slowly as β decreases. The difficulty in obtaining even a steady-state solution of this kind, via any time-marching process was envisaged by Smith (1984).

Although this fully explains the difficulties encountered in the linearized case, it does not explain directly the eventual lack of convergence of our nonlinear computations. To gain some clues to this, let us return to our comparison of figure 10 (a, b). Beyond $k \doteqdot -3.25$ the linearized distribution (figure 10b) becomes negligible; the nonlinear distribution (figure 10a), however, exhibits a further peak in amplitude (somewhat smaller than the previous peak) at around $k = -5$, and a third (smaller) peak at around $k = -7.5$. This indicates that the nonlinearity is causing a rapid growth of higher-order modes. Inspection of distributions at earlier times (not

presented here) reveals that these modes grow very rapidly in time. There appears to be several possible explanations for the eventual failure of the nonlinear calculation to converge. The first is that the fast-Fourier-transform routine (which is in essence a trapezoidal quadrature) is unable to handle these increasingly larger and more rapid oscillations accurately. A second possible explanation is that downstream-growing waves triggered in the start-up process are culminating in a breakdown of the governing equations, perhaps similar to the type found in the large-h supersonic examples. A further related possibility (kindly pointed out by a referee) is that the higher-frequency modes will be the fastest-moving modes, and consequently will appear downstream sooner. Indeed, during the early stages of the computations, there were some signs of quickly moving (but extremely small-amplitude) ripples, which were fairly sensitive to grid size. As the k-grid is refined, progressively higher-frequency modes will be incorporated into the calculation, which will be propagated downstream with increasing wavespeed. Here a recent paper by Smith & Burggraf (1985) may be relevant, in which a treatment of high-frequency disturbances on a Blasius boundary layer was studied. Far downstream it was shown that flow disturbances ultimately become governed by the Benjamin–Ono equation, or at higher frequencies by the full Euler equations, involving probable bursts of vorticity from a viscous sublayer.

Let us now return to considering sinusoidal time-varying distortions. (Notice that figure 8(a, b) just shows remnants of the transient waves described above at $t = \frac{1}{2}\pi$, $X \doteq 5$.) In particular we shall be interested in the effect of nonlinearity on the time-periodic solution. It is rather difficult to quantify this on results of this kind; however, we chose to trace the downstream development of a single maximum ('crest') or minimum ('trough') in the perturbation-wall-shear distribution (we could equally well have chosen any other physical quantity), these 'troughs' and 'crests' being wavelike in nature. Figure 12 shows just such a development for a number of different values of h; here all magnitudes are normalized with respect to $-|h|$. All results on this figure were obtained using the fine grid I, and all relate to $\beta = 1$.

The first set of results (denoted by the symbol □) is for the linearized case. Associated with each symbol is the corresponding time. Although we cannot be completely sure how the transient solution affects these distributions (as noted earlier the computation for this case became unreliable before one complete cycle of hump oscillation had been completed), the decaying nature of the wave downstream indicates that transient terms are likely to be of secondary importance. This decay downstream is in line with our linearized analysis in §2, for this choice of β, and adds further credibility to our numerical results.

Let us now turn for comparison to nonlinear results. Symbol △ shows the development of a wave trough for $h = 1$. Although the magnitude initially decays, after $X \doteq 5.5$ (corresponding to $t = 3.705$), the wave magnitude begins to grow. Now it is difficult to be completely conclusive about this feature, partly because of the uncertainty regarding the decay of the transient solution, and partly because the computation became unreliable owing to increasingly large oscillations (and ultimately failed) soon after the last timestep shown. All the results shown in figure 12 are at times before the computation became noticeably unreliable. For $h = 1$, these results strongly suggest that nonlinearity has a generally destabilizing effect on the flow. Although in this example $\beta = 1 > \beta_c$, supercritical modes appear to be triggered through nonlinearity, resulting in a wave-amplitude growth downstream.

Since is was not possible to investigate the expected following wave 'crest' in the wall-shear-perturbation distribution, instead we next took $h = -1$, and the symbol
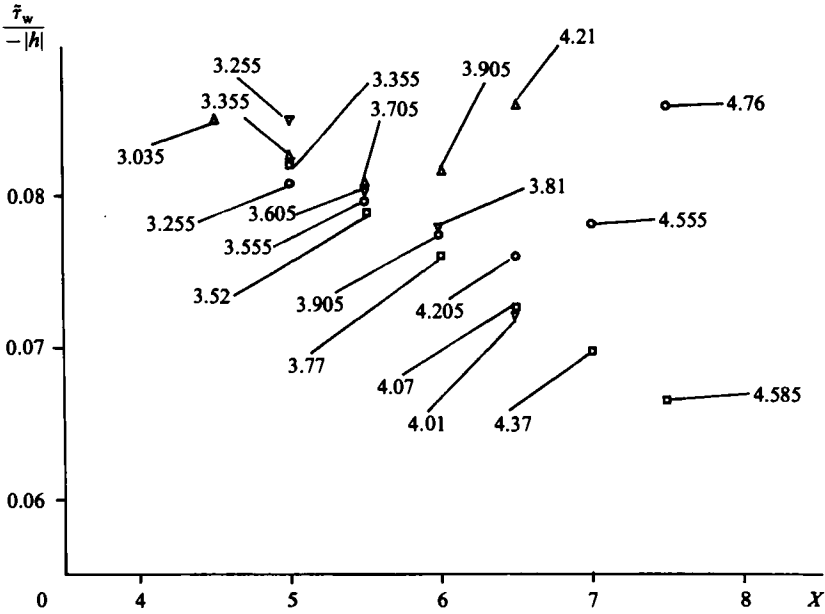
FIGURE 12. Development of perturbation wall shear; maximum wave magnitude (normalized with respect to $-|h|$), $\beta = 1$: $\square$, linear case; $\triangle$, $h = 1$ (nonlinear case); $\triangledown$, $h = -1$ (nonlinear case); $\bigcirc$, $h = \frac{1}{2}$ (nonlinear case). Numbers associated with each symbol denote time.

$\triangledown$ shows the development of the wave 'crest' corresponding to the 'troughs' in the previous two examples. The amplitude is seen to decay with X (and t) up to at least $X = 6.5$, nonlinearity enhancing this decay slightly when compared to the linear results.

As a final example for $\beta = 1$ we took $h = \frac{1}{2}$, and results for the shear trough are indicated on figure 12 by the symbol $\bigcirc$. As in the $h = 1$ nonlinear example the amplitude decays before seeming to grow. Again a note of caution is in order here because of the difficulties with the reliability of the solution (this particular computation eventually failed at $t \doteq 5.5$). The station where the turnaround from decay to growth occurs (akin to a neutrally stable point) has moved downstream (to $X \approx 6.5$) when compared to the $h = 1$ nonlinear results. This trend was confirmed by other results (not presented here), for other choices of h. This trend seems physically realistic; as $h \to 0$ the nonlinear solution will approach the linearized solution, i.e. will decay further and further downstream before the unstable modes eventually become significant and lead to a growth in the solution.

The final case presented for which $\beta > \beta_c$, is the nonlinear example for $h = 1$, $\beta = 0.7$, and figure 13 shows the development of a wave 'trough' in the perturbation-wall-shear distribution (obtained on grid I). This clearly shows a growing wave downstream for this frequency of oscillation, which according to linearized theory should be subcritical. The linearized solution was also generated in this grid, and these results (not shown) produce a decaying solution downstream, in line with our theory of §2. The nonlinear results, then, indicate that nonlinearity can trigger unstable solution modes for $\beta > \beta_c$. As expected from (4.17), the computation for this smaller value of β proceeded for a longer time than the $\beta = 1$ case, before the computation became unreliable and failed.

We next turn our attention to a value of β which, according to linearized theory,
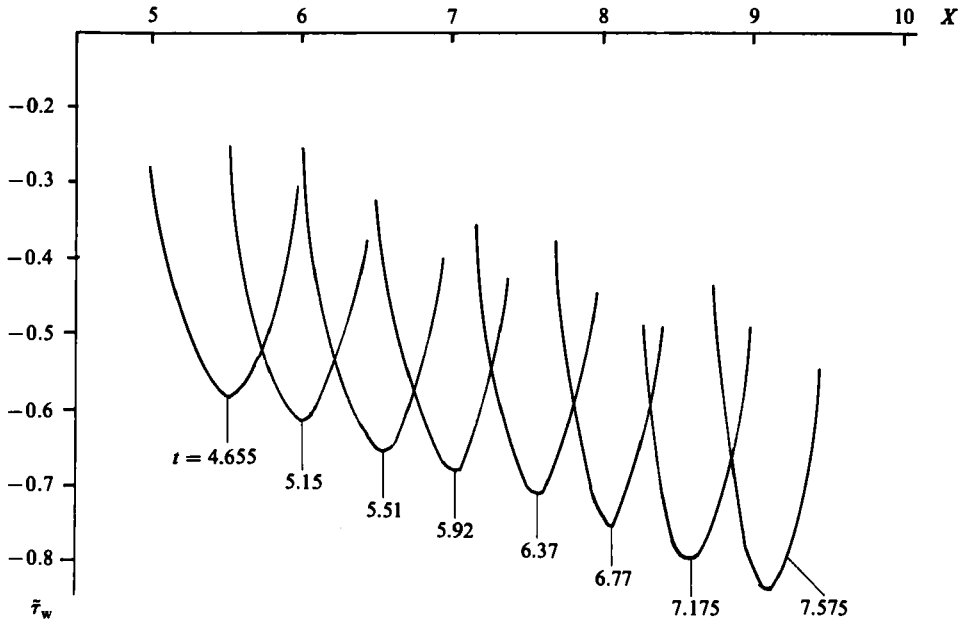
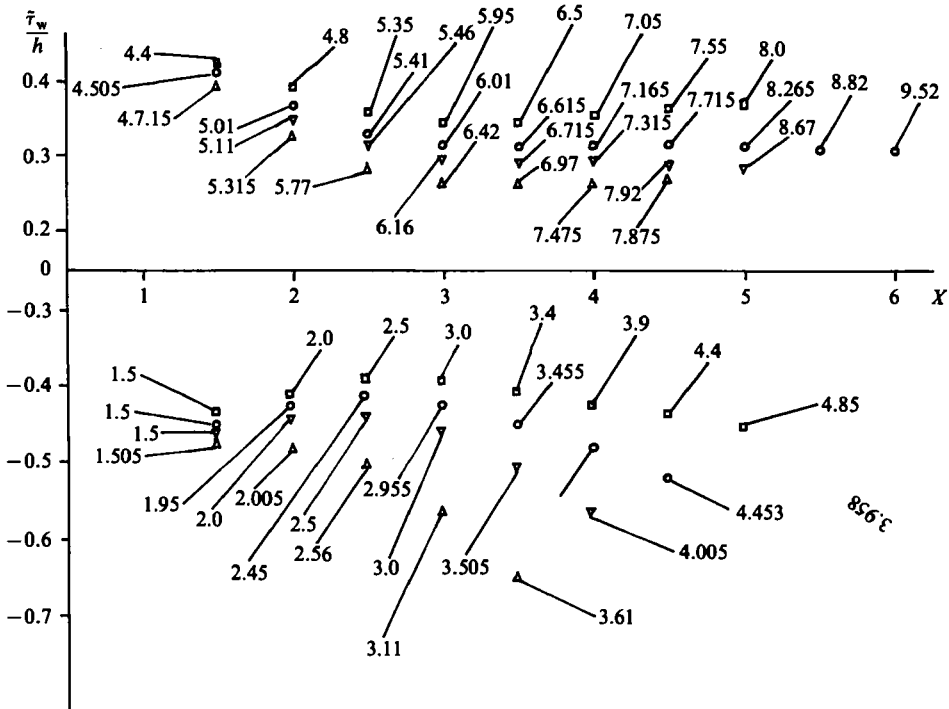FIGURE 13. Wave trough development $h = 1$, $\beta = 0.7$ (nonlinear case).

FIGURE 14. Development of perturbation wall shear: maximum wave magnitude (normalized with respect to h), $\beta^2 = 0.4$: $\square$, linear case; $\triangle$, $h = 1$ (nonlinear case); ∇, $h = \frac{1}{2}$ (nonlinear case); $\bigcirc$, $h = \frac{1}{4}$ (nonlinear case). Numbers associated with each symbol denote time.

should be slightly supercritical, namely $\beta^2 = 0.4$ ($\beta \doteq 0.63$). In particular we shall investigate the effect of nonlinearity by again focusing on the development, downstream, of a single maximum/minimum in the perturbation-wall-shear distribution. The results are shown in figure 14 (where the amplitudes of the wave are normalized with respect to h). All results were obtained on grid I. Because these calculations remained reliable for much longer than the $\beta = 1$ examples, we are able to show both a wave 'trough' and the following wave 'crest'.

The symbol $\square$ denotes the linearized results. These confirm the slightly supercritical nature of the flow, as predicted by our linearized theory in §2, and provide a (partial) check on our numerical method (although it does not, of course, check our computation of the nonlinear terms). Notice that the difference in magnitude between the 'troughs' and 'crests' gives us a fairly good indication of the effect of transient terms on the solution as the 'fully developed' linearized solution would have 'troughs and crests' of the same magnitude, separated by π in time, at the corresponding X-station.

The remainder of the results on figure 14 are nonlinear. It has been shown by Smith (1979a) that, for very slightly supercritical disturbances (which are small on the scale of the lower deck, i.e. $h \to 0$), nonlinearity has a stabilizing influence on the solution. We next seek to confirm these results from weakly nonlinear-stability theory.

Nonlinear results for $\beta^2 = 0.4$ and $h = 1, \frac{1}{2}, \frac{1}{4}$ are denoted by the symbols $\triangle$, $\triangledown$ and $\bigcirc$ respectively on figure 14. A number of observations are immediately apparent. The effect of nonlinearity on the negative perturbation wall shear is generally to increase its magnitude, compared with the linearized case (i.e. a generally destabilizing influence). On the other hand, its effect on the 'crests' is generally to reduce their magnitude somewhat (i.e. a stabilizing influence), although there was some evidence, albeit rather inconclusive, that far enough downstream the wave crests would also eventually grow in amplitude. Interestingly enough, this is the reverse of the usual effect of nonlinearity in steady flows.

The stabilizing effect of the nonlinearity on wave 'crests' in the shear distributions, as seen in the nonlinear results of figure 14, is in broad qualitative agreement with the weakly nonlinear predictions of Smith (1979a). The correlation between this theory and the effect of nonlinearity on the wave 'troughs' of the perturbation wall shear is not quite so clear, and requires rather closer observation and interpretation of the results. In the nonlinear case of $h = 1$ the 'trough' magnitude is seen to increase continuously; in the case of $h = \frac{1}{4}$ the wave 'trough' initially decays in amplitude before ultimately growing. The results for $h = \frac{1}{4}$ are initially very similar to those expected from linearized theory, although, once the wave starts to grow, its growth is much more rapid than the linearized case, presumably because of the growth of higher-order modes triggered through the nonlinear interaction.

Perhaps the most interesting case shown is that of $h = \frac{1}{2}$. This indicates that initially the wave is practically of constant amplitude (with less 'dip' in magnitude than observed in the linearized case) before the amplitude begins to grow. We may surmise that this amplitude plateau is related to the predictions of weakly nonlinear theory (although quantitative comparison is difficult).

The situation regarding slightly supercritical values of β (according to linearized theory) is then as follows: in the linear case, the wave amplitudes are seen initially to decay downstream, before growing, with the position of the neutral point moving further downstream as $\beta \to \beta_c$ (from below). The particular details of this changeover from decay to growth will be partly determined by the distortion shape under consideration. In the case of 'crests' in the wall shear distribution, nonlinearity
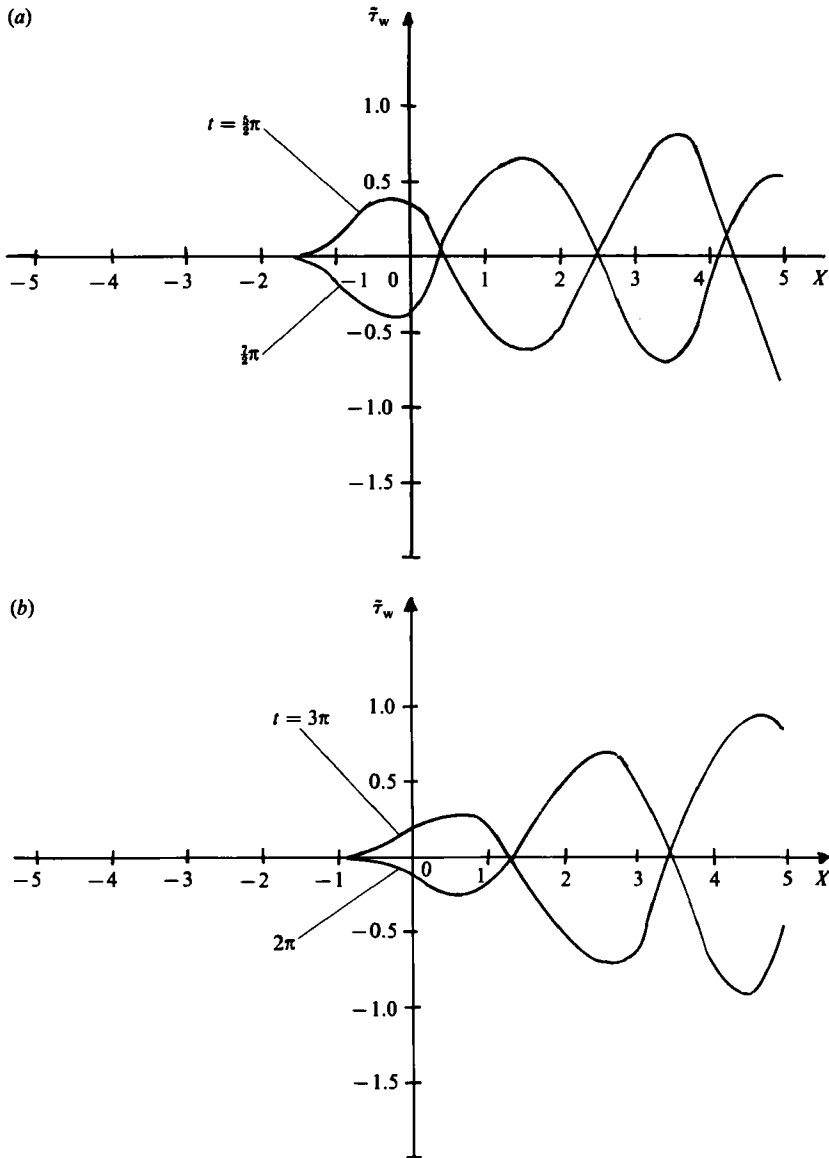
(a)

(b)

FIGURE 15(a, b). For caption see facing page.

tends to reduce wave amplitudes (at least in the early stages of the development), with obvious parallels with weakly nonlinear theory. In the case of 'troughs' non-linearity tends to increase wave amplitudes. However if $\beta - \beta_c$ is small and the magnitude of h is chosen appropriately relative to $\beta - \beta_c$ (according to Smith 1979a, $h = O(|\beta - \beta_c|^{\frac{1}{2}})$), then the effect of nonlinearity seems to 'level out' the dip in amplitude observed in the linearized case. If h is too small relative to $\beta - \beta_c$, then the effect of nonlinearity is insufficient, and the solution takes on more of the linearized form, as evidenced by the $h = \frac{1}{4}$ results on figure 14. If h is too large relative to $\beta - \beta_c$, then nonlinearity dominates and leads to a continuously growing 'trough' amplitude; this is illustrated by the $h = 1$ nonlinear results on figure 14. For weakly nonlinear results
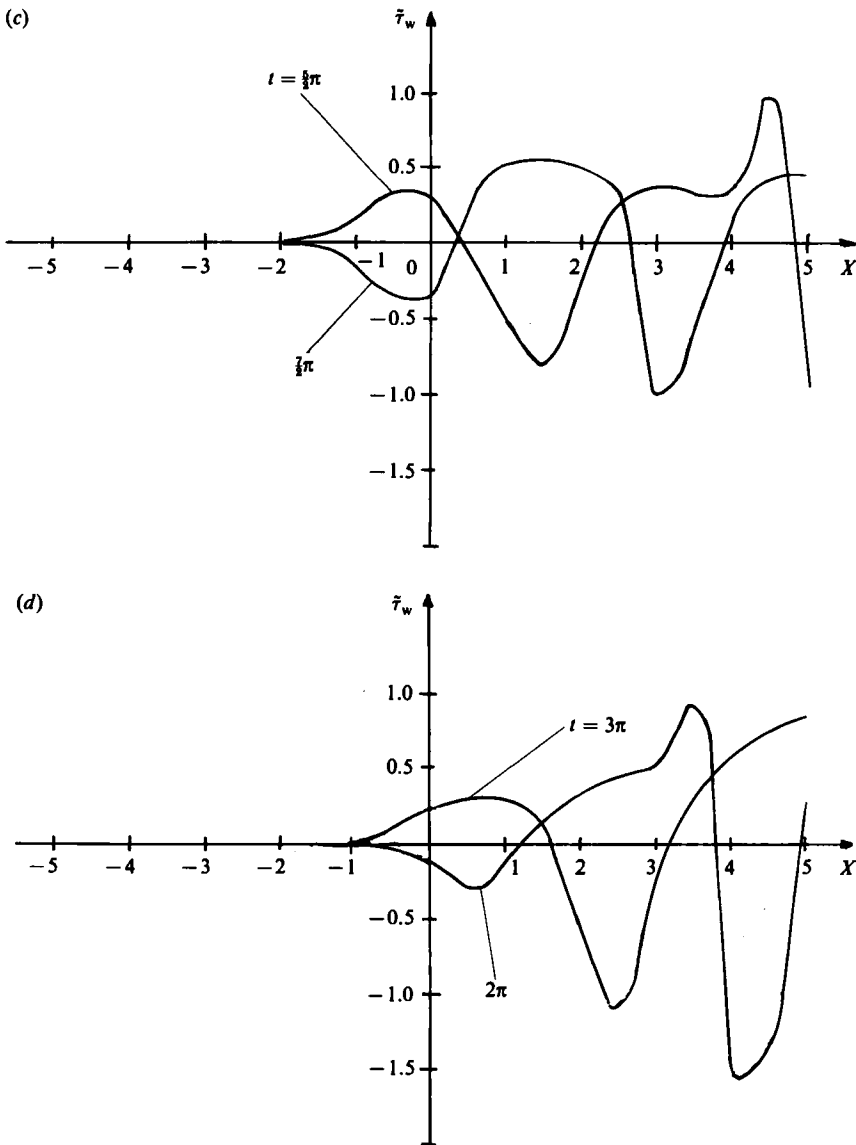
FIGURE 15. Spatial distribution of perturbation wall shear $h = 1$,
$\beta = \frac{1}{2}$. (a, b) linear results; (c, d) nonlinear results.

to apply, h must be chosen correctly. For $\beta^2 = 0.4$, of the three values of h investigated, $h = \frac{1}{2}$ appears to give the flattest amplitude plateau. Further down-stream higher-order modes take effect and the solution eventually grows in amplitude (see also the comments of Smith 1984). Overall it is perhaps a little misleading to interpret the effect of nonlinearity as being a stabilizing influence because of the manner in which the amplitude plateau forms in the case of 'troughs' in the wall-shear distribution. However, our analogy with the homogeneous (i.e. stability) problem is not perfect, as here we are exciting all values of k, rather than just a single value. Finally, although we have concentrated solely on waves arising in the perturbation-wall-shear distribution, we could have equally well have focused our
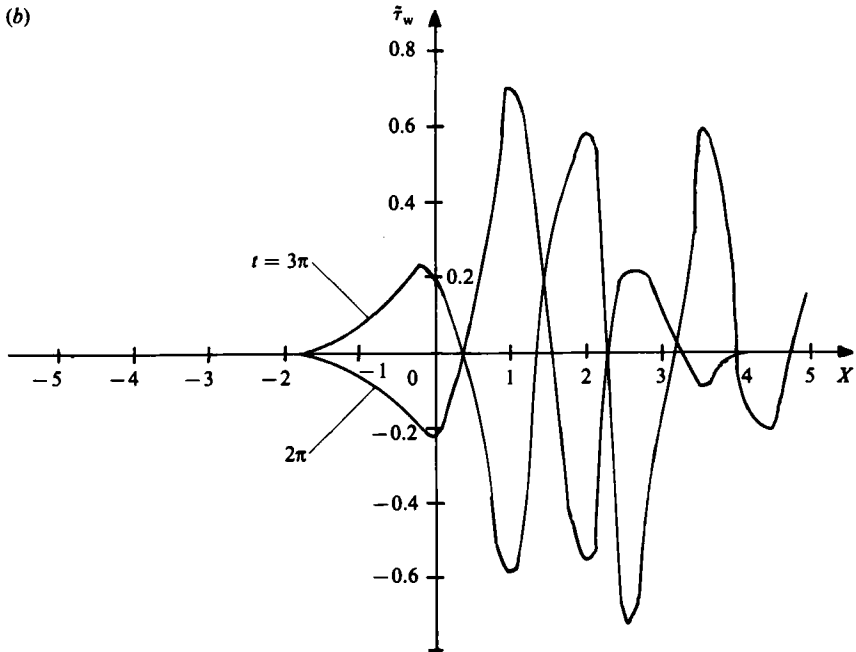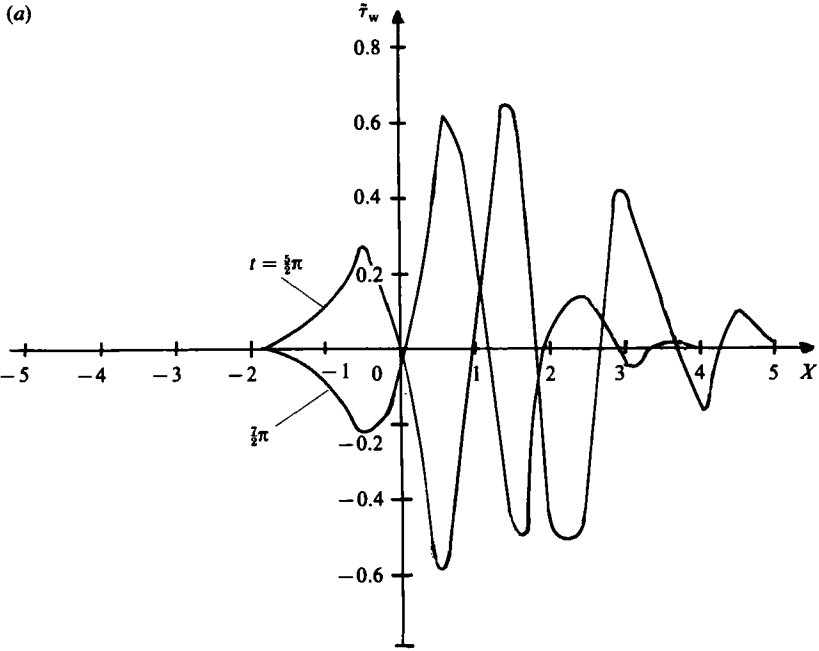
(a)

$\tilde{\tau}_w$

0.8

0.6

0.4

$t = \frac{5}{2}\pi$

0.2

$\frac{7}{2}\pi$

−0.2

−0.4

−0.6

−5 −4 −3 −2 −1 0 1 2 3 4 5 X

(b)

$\tilde{\tau}_w$

0.8

0.6

0.4

$t = 3\pi$

0.2

2π

−0.2

−0.4

−0.6

−5 −4 −3 −2 −1 0 1 2 3 4 5 X

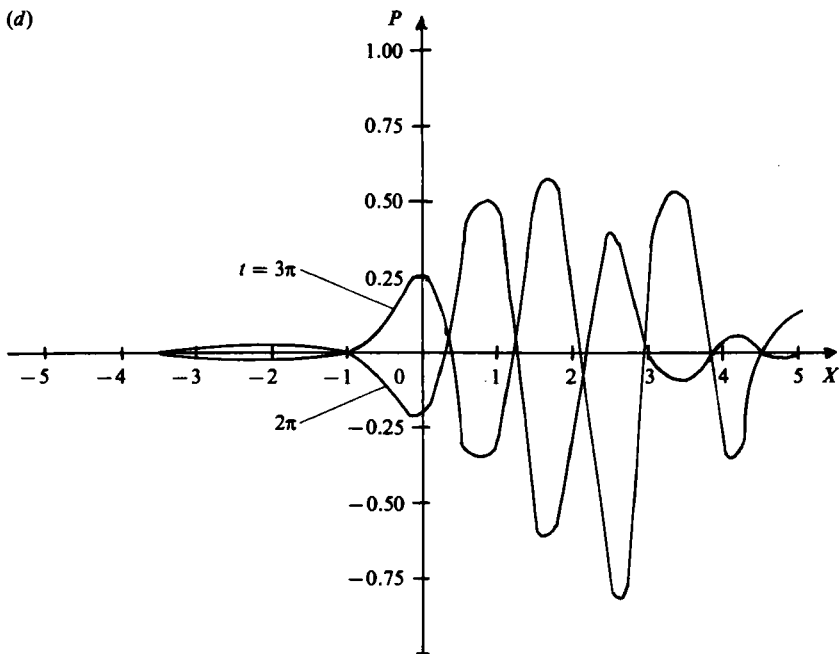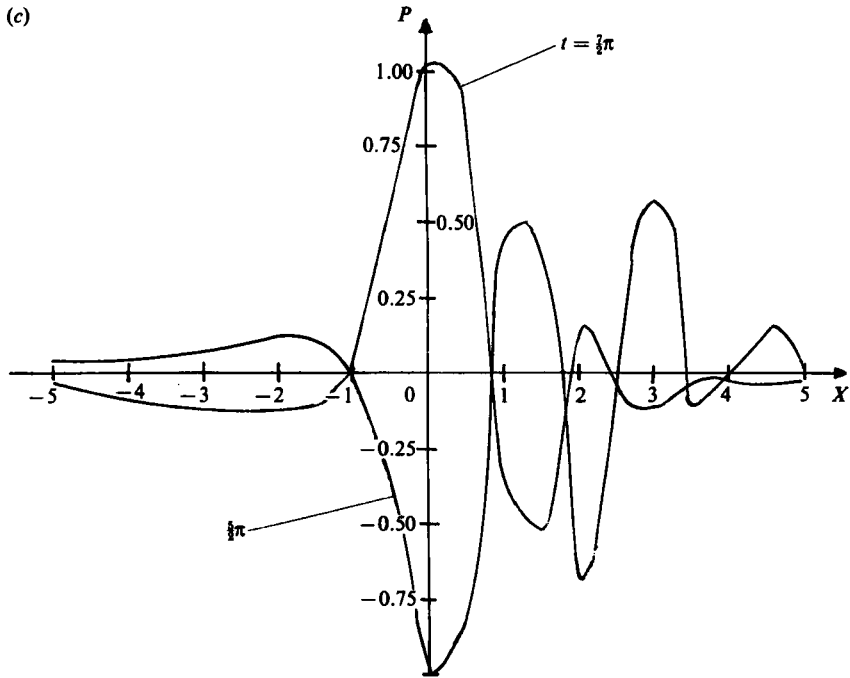FIGURE 16(*a, b*). For caption see facing page.

(c)

(d)

FIGURE 16. (a, b) Spatial distribution of perturbation wall shear; (c, d) spatial distribution of pressure: $h = 1$, $\beta = \frac{1}{4}$ (nonlinear results).

attention on any of the other physical quantities evaluated, which all exhibit similar wave-like forms in their distributions.

We conclude this section with results from two further examples that are supercritical according to linearized theory. Figure 15(a, b) shows the linearized perturbation-shear distributions at the wall for $h = 1$, $\beta = \frac{1}{2}$ (obtained on the coarser grid II), whilst figure 15(c, d) shows the corresponding nonlinear results (obtained using grid I). The growing-amplitude waveforms are clearly visible in both cases. The linearized results again give us an estimate for the effect of the transient solution by comparing the magnitude of the solution at time steps π apart (this appears to be fairly negligible). The effect of nonlinearity is observed to be broadly as before, namely of tending to reduce the amplitude of the perturbation-wall-shear wave crests, but generally amplifying the troughs. This nonlinear calculation failed at $t \approx 11.68$, in the manner described for the previous examples. Further, these nonlinear results were checked using a control computation on grid II. Up to around $t = \frac{5}{2}\pi$ the two sets of results agree to graphical accuracy, although at this time the control computation did show initial signs of oscillating far upstream. By $t = 3\pi$ this discrepancy had grown to around 10 % and even the grid I results were showing signs of oscillation. The control computation again failed at about the same time as the grid I calculation.

The final example computed was for $h = 1$, $\beta = \frac{1}{4}$. The (nonlinear) results obtained on grid I are shown in figure 16(a, b) (perturbation wall shears) and figure 16(c, d) (pressures). Although downstream-growing waves are being created, compared with the previous set of results (for $\beta = \frac{1}{2}$) these waves are rather smaller in amplitude, and are of rather smaller wavelength; additionally, the waves grow rather more slowly than in the $\beta = \frac{1}{2}$ case. These trends are confirmed by the linearized analysis in §2. It is likely, however, that the transient solution will still be quite significant, because of the smallness of β.

For this class of distortion, as $\beta \to 0$, I predicts

$$P = \frac{h(X^2 - 1) \sin t}{(1 + X^2)^2} + O(\beta^2),$$ (4.21)

$$\tilde{\tau}_w = \frac{2Xh\beta(3 - X^2) \cos (t + \frac{1}{4}\pi)}{(1 + X^2)^3} + O(\beta^2)$$ (4.22)

(correcting a sign error in I). From upstream, up to around $X = 1$, comparison of figures 15 and 16 does confirm a trend towards these results, although the results of I can give no indication of the creation of the growing waves, which as $\beta \to 0$ only become significant far downstream. This computation showed no signs of failure before the calculation was terminated ($t \approx 3\pi$), but we believe that, had the computation proceeded further, failure would eventually have occurred. Here again, the far-downstream, high-frequency analysis of Smith & Burggraf (1985) may be relevant.

5. Conclusions

By studying the fully nonlinear problem (1.6) we have obtained results for the nonlinear-(incompressible-)boundary-layer-stability problem, somewhat further from neutral points on the lower branch than is given by weakly nonlinear theory. Our results indicate that, in general, nonlinearity has destabilizing effect on boundary layers, whilst at the same time we believe we have confirmed certain of the predictions of weakly nonlinear-stability theory, although this does require very careful choice

of parameters. The general effect of this nonlinear destabilization is illustrated for choices of β greater than β_c (the critical value according to linearized theory) for which the flow disturbances ultimately appear to grow downstream, although it is difficult to assess the terminal behaviour of these (or indeed of any of the growing) solutions far downstream.

Our numerical scheme does experience difficulties, due primarily to the start-up process of the hump movement, which always triggers all time modes (including unstable modes), even in the linearized case, and leads to an increasing-amplitude wave packet downstream. Although this is a restriction on the method, it is likely that conventional (i.e. finite-difference) schemes would experience alternative difficulties as a result of this growing start-up wave, presumably at large distances downstream of the distortion.

For the supersonic case none of these difficulties exist, all modes of disturbance seem to decay downstream, and our numerical scheme yields solutions (including those with reversed flow) simply and efficiently. However, for sufficiently large humps, what appears to be a Rayleigh type of instability can occur, owing to non-linear effects entirely, culminating in a breakdown of the governing equations, with the result that our numerical scheme then becomes ill-posed. Conventional finite-difference schemes also face the same difficulties under similar circumstances (see Duck 1985). Presumably there exists an envelope (in (h, β)-space) inside which such a breakdown develops. For $\beta = 1$, for the particular choice of distortion taken, the critical value of h lies between 7.5 and 10.

There is every reason to suspect that the same phenomenon will occur in the incompressible case for large enough h (at least within a range of β). However, because of the difficulties involved with the Tollmien–Schlichting instability in this case, it would appear to be quite a difficult numerical task to generate such an effect (although, as suggested in the previous section, just such a breakdown may be caused by the start-up process).

To conclude, these results indicate (at least in this problem) an intimate relationship between the phenomena of Tollmien–Schlichting instability, (probable) Rayleigh-type instability, and unsteady (and sometimes catastrophic) separation, with all these effects being observed within the single framework of the triple-deck model.

REFERENCES

BOGDANOVA, E. V. & RYZHOV, O. S. 1983 Free and induced oscillations in Poiseuille flow. *Q. J. Mech. Appl. Maths* **36**, 271.

BURGGRAF, O. R. & DUCK, P. W. 1981 Spectral computation of triple deck flows. In *Proc. Symp. Phys. Num. Aspects in Aerodyn. Flows, California State University, Long Beach.* Springer.

COOLEY, J. W. & TUKEY, J. W. 1965 An algorithm for the machine computation of complex Fourier series. *Math. Comp.* **19**, 297.

DANIELS, P. G. 1974 Numerical and asymptotic solutions for the supersonic flow near the trailing edge of a flat plate at incidence. *J. Fluid Mech.* **63**, 641.

DUCK, P. W. 1978 Laminar flow over a small unsteady hump on a flat plate. *Mathematika* **25**, 24.

DUCK, P. W. 1981 Laminar flow over a small unsteady three-dimensional hump. *Z. angew. Math. Phys.* **32**, 62.

DUCK, P. W. 1984 The effect of a surface discontinuity on an axisymmetric boundary layer. *Q. J. Mech. Appl. Maths* **37**, 57.

DUCK, P. W. 1985 Pulsatile flow through constricted or dilated channels: Part II. *Q. J. Mech. Appl. Maths* (in press).

DUCK, P. W. & BURGGRAF, O. R. 1985 Spectral solutions for three-dimensional triple-deck flow over surface topography. *J. Fluid Mech.* (in press).

JOBE, C. E. & BURGGRAF, O. R. 1974 The numerical solution of the asymptotic equations of trailing-edge flow. *Proc. R. Soc. Lond.* A **340**, 91.

LIN, C. C. 1955 *Theory of Hydrodynamic Stability.* Cambridge University Press.

RIZZETTA, D. P., BURGGRAF, O. R. & JENSON, R. 1978 Triple deck solutions for viscous supersonic and hypersonic flow past corners. *J. Fluid Mech.* **89**, 535.

RYZHOV, O. S. & ZHUK, V. I. 1980 Internal waves in the boundary layer with the self-induced pressure, *J. Méc.* **19**, 561.

SMITH, F. T. 1973 Laminar flow over a small hump on a flat plate. *J. Fluid Mech.* **57**, 803.

SMITH, F. T. 1979 *a* Nonlinear stability of boundary layers for disturbances of various sizes. *Proc. R. Soc. Lond.* A **368**, 573. See also *Proc. R. Soc. Lond.* A **371**, 439.

SMITH, F. T. 1979 *b* On the non-parallel flow stability of the Blasius boundary layer. *Proc. R. Soc. Lond.* A **366**, 91.

SMITH, F. T. 1984 Theoretical aspects of steady and unsteady laminar separation. *A.I.A.A. paper* 84-1582.

SMITH, F. T. & BURGGRAF, O. R. 1985 On the development of large-sized short-scaled disturbances in boundary layers. *Proc. R. Soc. Lond.* (in press).

STEWARTSON, K. & WILLIAMS, P. G. 1969 Self induced separation. *Proc. R. Soc. Lond.* A **312**, 181.

STUART, J. T. 1960 On the non-linear mechanics of wave disturbances. Part 1. The basic behaviour in plane Poiseuille flow. *J. Fluid Mech.* **9**, 353.

TERENTEV'EV, E. D. 1978 On an unsteady boundary layer with self-induced pressure in the vicinity of a vibrating wall in a supersonic flow (in Russian). *Dokl. Akad. Nauk SSSR* **240**, 1046.

TUTTY, O. R. & COWLEY, S. J. 1985 Stability and numerical solution of the unsteady interactive boundary-layer equation *J. Fluid Mech.* (in press).

VELDMAN, A. E. P. 1979 The calculation of incompressible boundary layers with strong viscous–inviscid interaction. *Rep. NLR-Tr* 79023 Nat. Aerosp. Lab., Netherlands.

WATSON, J. 1960 On the non-linear mechanics of wave disturbances in stable and unstable parallel flows. Part 2. The development of a solution for plane Poiseuille flow and Couette flow. *J. Fluid Mech.* **9**, 371.

WILLIAMS, P. G. 1975 A reverse flow calculation in the theory of self-induced separation. In *Proc. 4th Intl Conf. Num. Meths in Fluid Dyn.* Lecture Notes in Physics, vol. 35, p. 445. Springer.

ZHUK, V. I. & RYZHOV, O. S. 1978 On one property of the linearized boundary-layer equations with a self-induced pressure (in Russian). *Dokl. Akad. Nauk SSSR* **240**, 1042.